

# Simulation of airflow past a 2D NACA0015 airfoil using an isogeometric incompressible Navier-Stokes solver with the Spalart-Allmaras turbulence model

Knut Nordanger<sup>a,\*</sup>, Runar Holdahl<sup>b</sup>, Trond Kvamsdal<sup>a,b</sup>, Arne Morten Kvarving<sup>b</sup>, Adil Rasheed<sup>b</sup>

<sup>a</sup>*Department of Mathematical Sciences, Norwegian University of Science and Technology, NO-7491 Trondheim, Norway*

<sup>b</sup>*SINTEF ICT, Department of Applied Mathematics, Postboks 4760 Sluppen, NO-7465 Trondheim, Norway*

---

## Abstract

The work presented in this paper concerns the efforts of conducting a computational fluid dynamics (CFD) simulation of air flow past a fixed 2D NACA0015 airfoil at high Reynolds number ( $Re = 2.5 \times 10^6$ ) using an isogeometric finite element methodology with linear, quadratic and cubic spline elements. Flow simulations at such high Reynolds numbers require turbulence models or very high resolution. The present work employs the Spalart-Allmaras turbulence model combined with a Navier-Stokes solver based on a Chorin projection method, the first development of its kind in an isogeometric finite element framework. The obtained results from the simulations are compared with two sets of experimental results available in the literature.

*Keywords:* Isogeometric analysis, NACA0015 airfoil, Chorin projection method, Spalart-Allmaras

---

## 1. Introduction

Wind power has gained political momentum in recent years owing to its relatively lesser environmental conflicts, greater efficiency and favorable wind conditions. The European Union (EU), for example, has a slogan 20 – 20 – 20, which implies that by 2020 20 % of the EU's energy should come from renewable sources, greenhouse gas emissions should decrease by 20 % and energy efficiency should increase by 20 %. By that time it is expected that 40 GW of the offshore wind power capacity would have already been installed [1]. In 2013 alone, around 11100 MW of wind power infrastructures, both onshore and offshore, were installed in the EU [2]. Meanwhile, an increasing number of wind turbines have been and will be installed in both the United States (US) and China.

---

\*Corresponding author

*Email addresses:* `knut.nordanger@math.ntnu.no` (Knut Nordanger), `runar.holdahl@sintef.no` (Runar Holdahl), `trond.kvamsdal@math.ntnu.no` (Trond Kvamsdal), `arne.morten.kvarving@sintef.no` (Arne Morten Kvarving), `adil.rasheed@sintef.no` (Adil Rasheed)

Offshore wind energy compared to its onshore counterpart appears more attractive due to its lesser visual impact and lesser issues related to land acquisition. Relatively more convenient accessibility to open sea allows for the installation of larger and larger turbines capable of producing much more power resulting in far lesser number of turbines per wind farm to produce the same amount of power. However, the large size of the turbines and the harsh meteorological conditions offshore come with new design challenges, not appropriately addressed by the traditional engineering methods/tools [3]. One such problem is related to the dynamic loading and unloading of turbine blades and structures. Fluid-structure interaction (FSI) simulation tools are being developed to address the issue and have already become a reality for wind turbines ([4] and [5]) and bridges [6, 7, 8, 9]. However, such detailed 3D simulations are still computationally demanding and not suitable for performing sensitivity analysis for optimum blade design.

To strike a balance between accuracy and computational efficiency, inspiration can be taken from a strip theory approach which was used to simulate vortex-induced vibration of offshore risers and submerged pipelines in [8], [10] and [11]. In the approach, a series of 2D computational fluid dynamics (CFD) simulations were conducted to predict the flow characteristics around the riser and then the forces were transferred to the structure solver for finite element analysis using non-linear beam elements. The reliability of this method depends on the accuracy of the 2D simulations and hence as a starting point we investigate an approach based on isogeometric analysis which emerged in 2005 [12], and offers integration of analysis and CAD geometry [13] through the use of the same basis functions. This results in advantages such as better accuracy per degree-of-freedom and exact geometric representation.

Wind turbines have for many years been an active research field, and in recent years isogeometric wind turbine simulation results have been published by Bazilevs and others [14, 15, 4]. However, little has been published, barring some work like [16] and recently [17], on flow past a fixed airfoil. Moreover, most of the simulations in a wind engineering context using isogeometric analysis have been limited to Variational Multiscale (VMS) approach for modeling turbulence. Although the approach has a more sound basis for simulating turbulent flows, their applicability is somewhat constrained by their computationally expensive nature, i.e. need for doing 3D flow simulations.

A remedy in order to enable the use of 2D flow simulations is to use Reynolds-Averaged Navier-Stokes (RANS) equations with one-equation Spalart-Allmaras (SA) turbulence closure which has been specially developed and optimized for simulating 2D flow around airfoils [18]. Furthermore, based on a study by Valen-Sendstad et al. ([19]), that investigated the performance of six different solvers for incompressible flow, we have chosen to use a Chorin projection method (incremental pressure correction) as this was found to be the most efficient and accurate. This is further enhanced by applying Mineev stabilization for equal order elements [20]. We believe that the first step towards the use of strip theory is to develop and demonstrate a CFD solver based on splines (to improve geometric representation), with Chorin projection method (for efficiency) and Spalart Allmaras turbulence model (optimized for 2D flow around airfoils). The main contribution of this work is to demonstrate the seamless integration of geometry modeling, meshing and analysis tools using linear, quadratic and cubic spline elements and the achievable accuracy to simulate flow around a two-

dimensional NACA0015 airfoil.

## 2. Theory

A code intended for a task like sensitivity analysis / shape optimization requires it to be convenient to use and easy to make several runs by changing the input parameters. This requires a seamless integration of the geometry modeler, mesh generator and CFD solver. In this section we present a description of the NACA airfoils, governing equations of flow and turbulence modeling, their discretization, implementation of boundary conditions as well as equations used to compute the aerodynamic coefficients presented in the result section.

### 2.1. Introduction to 4-digit NACA airfoil

The family of symmetric NACA airfoils is denoted by NACA00XX where the last two digits give the ratio between the maximum thickness of the airfoil  $t$  and the chord length  $c$ . The shape of all NACA00XX airfoils is given by the analytical formula [21]

$$y_t = 5tc \left[ 0.2969 \sqrt{\frac{x}{c}} - 0.1260 \left(\frac{x}{c}\right) - 0.3516 \left(\frac{x}{c}\right)^2 + 0.2843 \left(\frac{x}{c}\right)^3 - 0.1015 \left(\frac{x}{c}\right)^4 \right] \quad (1)$$

where  $y_t$  is the distance from the centerline,  $t$  the maximum thickness from the centerline,  $c$  the chord length and  $x$  the position along the chord from 0 to  $c$ . In order to have a closed curve and thickness  $y_t = 0$  at  $x = c$  one of the coefficients has to be modified as they do not sum to zero. We choose to modify the last coefficient (i.e. the coefficient in front of the highest order term) to  $-0.1036$  as this gives the smallest perturbation of the surface curve. Sometimes the blade profile is given in the form of coordinate data at discrete points along the surface. No matter how the data is obtained it is used to get a spline representation following the approach described in Section 2.5.3.

### 2.2. Fluid solver

This section describes the fluid solver through the governing equations, the isogeometric finite element approximation, the projection method employed and the boundary conditions.

#### 2.2.1. Governing equations

Viscous airflow at low Mach numbers is mathematically described by the incompressible Navier-Stokes equations. These equations can be written as

$$\begin{aligned} \frac{\partial \mathbf{u}}{\partial t} + \rho (\mathbf{u} \cdot \nabla) \mathbf{u} - \nabla \cdot \boldsymbol{\sigma}(\mathbf{u}, p) &= \rho \mathbf{f} \quad \text{in } \Omega \\ \nabla \cdot \mathbf{u} &= 0 \quad \text{in } \Omega. \end{aligned}$$

Here,  $\Omega \in \mathbb{R}^d$ ,  $d = 2, 3$ , is a suitable, sufficiently regular and open domain,  $\rho$  is the constant fluid density,  $p$  is the pressure,  $\mathbf{u}$  is the fluid velocity vector and  $\mathbf{f}$  is a volumetric body force. The Cauchy stress tensor can be written as

$$\boldsymbol{\sigma}(\mathbf{u}, p) = -p\mathbf{I} + 2\mu\boldsymbol{\epsilon}(\mathbf{u}),$$

where  $\mathbf{I}$  is the identity tensor and  $\mu$  is the dynamic viscosity and the strain rate  $\boldsymbol{\epsilon}$  is defined as

$$\boldsymbol{\epsilon}(\mathbf{u}) = \frac{1}{2} (\nabla \mathbf{u} + (\nabla \mathbf{u})^T).$$

Furthermore, we define  $\partial\Omega = \Gamma = \Gamma_D \cup \Gamma_N \cup \Gamma_M$  where  $\Gamma_D$  are the boundaries with Dirichlet conditions,  $\Gamma_N$  the boundaries with Neumann conditions  $\Gamma_M$  the boundaries with mixed conditions. Mixed boundary conditions are used in situations where the normal velocity components are given, usually zero, together with the tangential stresses can model symmetry planes and slip or friction conditions.

The variational formulation is expressed as: Find  $(\mathbf{u}, p) \in \mathbf{U} \times Q$  such that

$$\left( \rho \frac{\partial \mathbf{u}}{\partial t}, \mathbf{v} \right) + c(\mathbf{u}; \mathbf{u}, \mathbf{v}) + b(p, \mathbf{v}) + a(\mathbf{u}, \mathbf{u}) + b(q, \mathbf{u}) = f(\mathbf{v}) \quad (\mathbf{v}, q) \in \mathbf{V} \times Q. \quad (2)$$

Here, we have defined the spaces

$$\begin{aligned} \mathbf{U} &= \mathbf{H}_{\Gamma_D, \Gamma_M^\perp}^1(\Omega) = \{ \mathbf{v} \in \mathbf{H}^1(\Omega) \mid \mathbf{v} = \mathbf{u}_D \text{ on } \Gamma_D \text{ and } \mathbf{v} \cdot \mathbf{n} = u_\perp \text{ on } \Gamma_M \} \\ \mathbf{V} &= \mathbf{H}_{\Gamma_D, \Gamma_M^\perp, 0}^1(\Omega) = \{ \mathbf{v} \in \mathbf{H}^1(\Omega) \mid \mathbf{v} = 0 \text{ on } \Gamma_D \text{ and } \mathbf{v} \cdot \mathbf{n} = 0 \text{ on } \Gamma_M \} \\ Q &= L^2(\Omega), \end{aligned}$$

where  $\mathbf{u}_D$  and  $u_\perp$  both are given functions and  $\mathbf{n}$  is the unit outer normal on  $\Gamma$ , and the forms

$$\begin{aligned} a(\mathbf{u}, \mathbf{v}) &= 2 \int_{\Omega} \mu \boldsymbol{\epsilon}(\mathbf{u}) : \boldsymbol{\epsilon}(\mathbf{v}) \, d\mathbf{x} \\ b(q, \mathbf{v}) &= - \int_{\Omega} (\nabla \cdot \mathbf{v}) q \, d\mathbf{x} \\ c(\mathbf{w}; \mathbf{u}, \mathbf{v}) &= \int_{\Omega} \rho (\mathbf{w} \cdot \nabla) \mathbf{u} \cdot \mathbf{v} \, d\mathbf{x} \\ f(\mathbf{v}) &= \int_{\Omega} \rho \mathbf{f} \cdot \mathbf{v} \, d\mathbf{x} + \int_{\Gamma_N} \mathbf{t} \cdot \mathbf{v} \, d\mathbf{s}, \end{aligned}$$

where  $\mathbf{t} = \boldsymbol{\sigma} \cdot \mathbf{n}$  is the traction vector on  $\Gamma$ . Here  $\mathbf{U}$  and  $\mathbf{V}$  are the velocity trial and test function spaces, respectively, whereas  $Q$  is the corresponding function spaces for the trial and test pressure variables. The velocity trial function space  $\mathbf{H}_{\Gamma_D, \Gamma_M^\perp}^1(\Omega)$  has the same regularity as the classical Hilbert space  $\mathbf{H}^1(\Omega)$  inside the domain  $\Omega$ , but restricted to fulfill the imposed Dirichlet conditions along  $\Gamma_D$  as well as mixed boundary conditions, see Section 2.2.4 along  $\Gamma_M^\perp$ . The velocity test function space  $\mathbf{H}_{\Gamma_D, \Gamma_M^\perp, 0}^1(\Omega)$  is similar to the velocity trial space, but have homogeneous Dirichlet conditions along  $\Gamma_D$  and  $\Gamma_M^\perp$ .

### 2.2.2. Isogeometric finite element approximation

The isogeometric finite element method approximates the solution by using a spline basis of polynomial order  $p$  and regularity  $C^{p-1}$ , whereas  $C^0$  Lagrange polynomials of low order (typical  $p = 1$  or  $p = 2$ ) are used in traditional finite

element formulations. Our approach is based on a conforming finite element approximation, i.e.

$$\mathbf{U}_h \subset \mathbf{U}, \quad \mathbf{V}_h \subset \mathbf{V}, \quad Q_h \subset Q.$$

The discrete approximation spaces  $\mathbf{U}_h, \mathbf{V}_h, Q_h$  are chosen as the isogeometric finite element spaces. This gives the semi-discrete formulation of the variational problem stated in Eq. (2): Find  $(\mathbf{u}_h, p_h) \in \mathbf{U}_h \times Q_h$  such that

$$\left( \rho \frac{\partial \mathbf{u}_h}{\partial t}, \mathbf{v}_h \right) + c(\mathbf{u}_h; \mathbf{u}_h, \mathbf{v}_h) + a(\mathbf{u}_h, \mathbf{u}_h) + b(p, \mathbf{v}_h) + b(q, \mathbf{u}_h) = f(\mathbf{v}_h)$$

for all  $(\mathbf{v}_h, q_h) \in \mathbf{V}_h \times Q_h$ .

Herein, we have developed a block-structured B-spline isogeometric finite element approximation of the Navier-Stokes equations described above. To construct a B-spline basis for a domain  $\Omega$  which is subdivided into a number of patches (a patch is equivalent to a block)  $\Omega_e$  such that  $\Omega = \cup_{e=1}^N \Omega_e$  we associate for each patch a knot-vector in each coordinate direction

$$\Xi_k^e = \left\{ \xi_{1,k}^e, \xi_{2,k}^e, \dots, \xi_{n_k^e + p_k^e + 1}^e \right\}$$

for  $k = 1, \dots, d$ . The B-spline basis for patch  $\Omega_e$  on the parametric domain  $\hat{\Omega} = (0, 1)^d$  is written as  $\hat{\mathcal{S}}_{\alpha^e}^{p^e}$  where the multi-indices  $\alpha^e = (\alpha_1^e, \dots, \alpha_d^e)$  and  $p^e = (p_1^e, \dots, p_d^e)$  denote the regularity and order for the basis in each coordinate direction, respectively. The corresponding basis for the physical domain  $\Omega_e$  can be expressed using the coordinate mapping  $\phi_e : \hat{\Omega} \rightarrow \Omega_e$  as

$$\mathcal{S}_{\alpha^e}^{p^e} = \left\{ v_h \mid v_h \circ \phi_e \in \hat{\mathcal{S}}_{\alpha^e}^{p^e} \right\}.$$

If the variational formulation allows a discontinuous approximation the spline finite element basis for the domain  $\Omega$  can be defined as

$$\mathcal{S}_h = \left\{ v_h \mid v_h|_{\Omega_e} \in \mathcal{S}_{\alpha^e}^{p^e} \right\}.$$

If we assume that the knot-vectors and geometrical mapping  $\phi_e$  for all the patches are consistent on common edges and faces we can define a continuous basis

$$\mathcal{S}_h = \left\{ v_h \in C(\Omega) \mid v_h|_{\Omega_e} \in \mathcal{S}_{\alpha^e}^{p^e} \right\}.$$

### 2.2.3. Projection method

In order to solve the mixed variational problem given above the following inf-sup condition

$$\inf_{q_h \in Q_h, q_h \neq 0} \sup_{\mathbf{v}_h \in \mathbf{V}_h, \mathbf{v}_h \neq 0} \frac{b(q_h, \mathbf{v}_h)}{\|q_h\|_{L^2(\Omega)} \|\mathbf{v}_h\|_{\mathbf{H}^1(\Omega)}} \geq C > 0.$$

needs to be satisfied in order to avoid spurious pressure modes [22]. This imposes restrictions on the choices of  $\mathbf{V}_h$  and  $Q_h$ .

Traditionally a mixed finite element method with different approximation spaces for pressure and velocity is required. In this work we use a pressure

correction projection scheme which allows for equal order approximation of the velocity and pressure. This is based on the work pioneered by Chorin [23] and Temam [24] in the late 1960s. However, the present implementation is inspired by the review article [25] which also accommodates significant progress regarding theoretical and implementational issues for projection schemes in recent years, and the work on pressure stabilization by Mineev as presented in [20].

For the chosen projection method one only needs to solve decoupled problems of elliptic equations at each time step instead of the full coupling of the velocity and pressure [25]. Thus standard Krylov subspace methods like the conjugate gradient (CG) method and Generalized Minimal RESidual method (GMRES) can be used to solve the linear systems. For these methods we also can employ efficient preconditioners. Drawbacks of the projection methods include a inherited splitting error and extra numerical boundary conditions for the pressure. This reduces the convergence order of the numerical approximation.

In order to avoid the inconsistent pressure boundary condition present in many splitting schemes one may choose a rotational formulation for the incremental pressure correction scheme as proposed in [26]. The resulting splitting error is now only due to an inaccurate slip condition imposed on the velocity. The rotational form of the Chorin splitting scheme is of order 2 for the velocity and order  $3/2$  for the pressure, both in the  $L^2$ -norm, [27]. However, in some of our numerical tests we observed pressure oscillations when we used equal order approximation. Thus, in order to get a stable solution with our equal order approximation we herein chose to employ Mineev stabilization as given in [20] to avoid node-to-node pressure oscillations.

The standard incremental pressure correction scheme is given by

1. Velocity prediction step

$$\begin{aligned} \frac{\rho}{2\Delta t} (3\tilde{\mathbf{u}}^{n+1} - 4\mathbf{u}^n + \mathbf{u}^{n-1}) + \rho (2\mathbf{u}^n - \mathbf{u}^{n-1}) \cdot \nabla \tilde{\mathbf{u}}^{n+1} \\ - \nabla \cdot \boldsymbol{\sigma}(\tilde{\mathbf{u}}^{n+1}, p^n) = \rho \mathbf{f}^{n+1}, \\ \tilde{\mathbf{u}}^{n+1} = 0 \text{ on } \Gamma. \end{aligned}$$

2. Pressure correction step

$$\begin{aligned} \frac{\rho}{2\Delta t} (3\mathbf{u}^{n+1} - 3\tilde{\mathbf{u}}^{n+1}) + \nabla (p^{n+1} - p^n) = 0, \\ \nabla \cdot \mathbf{u}^{n+1} = 0, \\ \mathbf{u}^{n+1} \cdot \mathbf{n} = 0 \text{ on } \Gamma. \end{aligned}$$

However, to get a stable solution without pressure oscillations for an equal order approximation Mineev [20] modified the pressure correction step and solved it in two successive steps

2.a Stabilized pressure correction (Galerkin formulation)

$$\begin{aligned} \left( \nabla \left[ (1 + \hat{\sigma})p^{n+1} - p^n \right], \nabla q \right) = -\frac{3}{2} (\nabla \cdot \tilde{\mathbf{u}}^{n+1}, q) \\ + \hat{\sigma} \left( \nabla \cdot (-2\mathbf{u}^n + \frac{1}{2}\mathbf{u}^{n-1}), q \right) \\ - \frac{\hat{\sigma}}{2} \int_{\partial\Omega} (3\tilde{\mathbf{u}}^{n+1} - 4\tilde{\mathbf{u}}^n + \mathbf{u}^{n-1}) \cdot \mathbf{n} q \, ds \quad q \in Q_h. \end{aligned}$$

Here,  $\hat{\sigma}$  is the stabilization parameter which is set equal to the time step in all simulations.

## 2.b Velocity correction

$$\frac{3}{2} (\mathbf{u}^{n+1} + \tilde{\mathbf{u}}^{n+1}) + \nabla (p^{n+1} - p^n) = 0$$

with boundary conditions as given in the problem formulation.

To summarize: Our algorithm implemented in IFEM is as follows:

1. Velocity prediction step  
Find  $\tilde{\mathbf{u}}^{n+1}$  using the velocities  $\mathbf{u}^n$  and  $\mathbf{u}^{n-1}$  and the pressure  $p^n$  computed at earlier time steps.
- 2.a Stabilized pressure correction (Galerkin formulation)  
Find  $p^{n+1}$  using the predicted velocity  $\tilde{\mathbf{u}}^{n+1}$  and the velocities  $\mathbf{u}^n$ ,  $\mathbf{u}^{n-1}$  and the pressure  $p^n$  computed at earlier time steps.
- 2.b Velocity correction  
Find  $\mathbf{u}^{n+1}$  using the predicted velocity  $\tilde{\mathbf{u}}^{n+1}$ , the updated pressure  $p^{n+1}$  and the pressure  $p^n$  computed at the previous time step.

The standard incremental pressure correction scheme is of order 2 for the velocity and order 1 for the pressure, both in the  $L^2$ -norm, [25]. As stated in [20], this is not changed when employing Mineev stabilization.

### Remark

The Pressure Poisson Equation (PPE) in Step 2.a implies that the proper discrete space  $Q_h$  for the pressure trial and test functions has to fulfill  $Q_h \subset L^2(\Omega) \cap H^1(\Omega)$ . Furthermore, in PPE we employ a homogeneous Dirichlet condition for the pressure at the outflow boundary and homogeneous Neumann conditions, i.e.  $\nabla p^{n+1} \cdot \mathbf{n}$  along the other boundaries.

#### 2.2.4. Boundary conditions

Several boundary conditions can be applied for the Navier-Stokes equations. We assume that  $\Gamma \subset \partial\Omega$  is a subset of the boundary of the domain. The Dirichlet and Neumann conditions can be written as

$$\begin{aligned} \mathbf{u} &= \mathbf{g} \text{ on } \Gamma \text{ (Dirichlet conditions)} \\ \boldsymbol{\sigma} \cdot \mathbf{n} &= \mathbf{h} \text{ on } \Gamma \text{ (Neumann conditions)}, \end{aligned}$$

where  $\mathbf{g} = \mathbf{g}(\mathbf{x}, t)$  and  $\mathbf{h} = \mathbf{h}(\mathbf{x}, t)$  are given functions and  $\mathbf{n}$  denotes the unit outer normal vector on  $\partial\Omega$ . Since only the gradient of the pressure is present in the Navier-Stokes equations and the Dirichlet condition does not involve any pressure information, the pressure can only be determined up to a constant if a Neumann condition is prescribed everywhere on the boundary. To fix the pressure level and have a well-defined problem a homogeneous pressure condition can be imposed on the outflow boundary. Furthermore, from the continuity condition we derive the following compatibility condition

$$\int_{\Omega} \nabla \cdot \mathbf{u} \, dx = \int_{\partial\Omega} \mathbf{u} \cdot \mathbf{n} \, ds = \int_{\partial\Omega} \mathbf{g} \cdot \mathbf{n} \, ds = 0,$$

i.e. the boundary condition must impose a zero mean flux on the boundary to satisfy mass conservation.

We now assume that the boundary  $\Gamma$  can be decomposed into three disjoint segments  $\partial\Omega = \partial\Omega_{\text{in}} \cup \partial\Omega_{\text{out}} \cup \partial\Omega_{\text{c}}$  with

$$\begin{aligned}\partial\Omega_{\text{in}} &= \{\mathbf{x} \in \Gamma \mid \mathbf{u} \cdot \mathbf{n} < 0\}, & (\text{inflow boundary}) \\ \partial\Omega_{\text{out}} &= \{\mathbf{x} \in \Gamma \mid \mathbf{u} \cdot \mathbf{n} > 0\}, & (\text{outflow boundary}) \\ \partial\Omega_{\text{c}} &= \{\mathbf{x} \in \Gamma \mid \mathbf{u} \cdot \mathbf{n} = 0\}, & (\text{characteristic boundary})\end{aligned}$$

On the inflow part of the boundary, i.e. on  $\partial\Omega_{\text{in}}$ , it is most natural to impose a Dirichlet condition. On outlet boundaries, i.e. on  $\partial\Omega_{\text{out}}$ , the Neumann condition is the preferred choice.

Mixed boundary conditions are also possible for the Navier-Stokes equations. A slip boundary condition can be written as

$$\begin{aligned}\mathbf{u} \cdot \mathbf{n} &= 0 \text{ on } \Gamma, \\ \mathbf{n} \cdot \boldsymbol{\sigma} \cdot (\mathbf{I} - \mathbf{n} \otimes \mathbf{n}) &= \mathbf{h} \text{ on } \Gamma,\end{aligned}$$

where  $\mathbf{I} - \mathbf{n} \otimes \mathbf{n}$  span the tangent plane to the boundary  $\partial\Omega$  in  $\mathbb{R}^d$ . This corresponds to a Dirichlet condition for the normal direction and a Neumann condition in the tangential plane.

### 2.3. Turbulence modeling

High Reynolds number flows are dominated by turbulence which can be fully resolved using Direct Numerical Simulation (DNS) or partially resolved using Large Eddy Simulation (LES). In LES the larger scales in the flow are resolved while the smaller scales are assumed to be isotropic and modeled using different kinds of subgrid scale parametrization. However, the computationally expensive nature of DNS and LES prohibits their usage as a design tool. It is one of the reasons that RANS models are still widely used. In the RANS model turbulence is not resolved but modeled. The mesh resolution and quality requirements for this class of models are also less stringent than the ones required in DNS or LES. In this work we employ the Spalart-Allmaras turbulence model [18] which has been optimized to simulate 2D flow around aerodynamically shaped bodies like an airfoil.

#### 2.3.1. The Spalart-Allmaras turbulence model

The Spalart-Allmaras turbulence model is a one-equation model for a modified turbulent kinematic viscosity  $\tilde{\nu}$  [18]. We employ the standard model presented in [18] along with the negative Spalart-Allmaras model presented in [28]. The formulation of the model is the transport equation

$$\frac{D\tilde{\nu}}{Dt} = P - D + \frac{1}{\sigma} \left[ \nabla \cdot ((\nu + \tilde{\nu}) \nabla \tilde{\nu}) + c_{b2} (\nabla \tilde{\nu})^2 \right],$$

where  $\nu = \mu/\rho$  is the laminar kinematic viscosity,  $\mathbf{u}$  is the fluid velocity and  $d$  is the distance from a given point to the closest solid wall. Furthermore, the production and wall destruction terms read

$$P = c_{b1}(1 - f_{t2})\tilde{S}\tilde{\nu}, \quad D = \left( c_{w1}f_w - \frac{c_{b1}}{\kappa^2}f_{t2} \right) \left[ \frac{\tilde{\nu}}{d} \right]^2.$$

The laminar suppression term  $f_{t2}$  is defined as

$$f_{t2} = c_{t3} \exp(-c_{t4}\chi^2),$$

with  $c_{t3} = 1.2$  and  $c_{t4} = 0.5$ . From the modified viscosity  $\tilde{\nu}$  the eddy viscosity can be computed as

$$\nu_t = \tilde{\nu} f_{v1}, \quad f_{v1} = \frac{\chi^3}{\chi^3 + c_{v1}^3}, \quad \chi \equiv \frac{\tilde{\nu}}{\nu}.$$

Modifications of the original model for the modified vorticity were published in [28]. The modified vorticity  $\tilde{S}$  is now given by

$$\bar{S} = \frac{\tilde{\nu}}{\kappa^2 \cdot d^2} f_{v2}, \quad f_{v2} = 1 - \frac{\chi}{1 + \chi f_{v1}},$$

where  $S$  represents the magnitude of the vorticity and  $d$  the distance to the closest wall, and

$$\tilde{S} = \begin{cases} S + \bar{S} & : \bar{S} \geq -c_{v2}S \\ S + \frac{S(c_{v2}S + c_{v3}\bar{S})}{(c_{v3} - 2c_{v2})S - \bar{S}} & : \bar{S} < -c_{v2}S \end{cases}$$

with  $c_{v2} = 0.7$  and  $c_{v3} = 0.9$ . The new modified vorticity  $\tilde{S}$  does not have the possibility of becoming negative and thus avoids a possible problem of disrupting other Spalart-Allmaras functions. Furthermore we have for the destruction term

$$\begin{aligned} f_w &= g \left[ \frac{1 + c_{w3}^6}{g^6 + c_{w3}^3} \right]^{1/6} \\ g &= r + c_{w2}(r^6 - r) \\ r &= \frac{\tilde{\nu}}{\tilde{S}\kappa^2 d^2}. \end{aligned}$$

In the original work [18] the following values are given for the other constants appearing in the model

$$\begin{aligned} c_{b1} &= 0.1355, & c_{b2} &= 0.622, & c_{w2} &= 0.3, & c_{w3} &= 2, \\ \sigma_{\tilde{\nu}} &= 2/3, & c_{\tilde{\nu}1} &= 7.1, & k &= 0.41. \end{aligned}$$

However, in cases with under-resolved grids and for some transient states, the produced  $\tilde{\nu}$  solution is negative. A typical choice is then to clip the negative  $\tilde{\nu}$  value, but we employ the negative Spalart-Allmaras model, presented in [28], which reads

$$\frac{D\tilde{\nu}}{Dt} = P_n - D_n + \frac{1}{\sigma} \nabla \cdot [(\nu + \tilde{\nu} f_n) \nabla \tilde{\nu}] + \frac{c_{b2}}{\sigma} (\nabla \tilde{\nu})^2,$$

where  $P_n$  is the production,  $D_n$  is the wall destruction and  $f_n(\chi)$  is diffusion coefficient modification. The diffusion coefficient modification is given as

$$f_n = \frac{c_{n1} + \chi^3}{c_{n1} - \chi^3},$$

where  $c_{n1} = 16$ . Furthermore we have

$$P_n = c_{b1}(1 - c_{t3})S\tilde{\nu}, \quad D_n = -c_{w1} \left[ \frac{\nu}{d} \right]^2,$$

where  $S$  is the vorticity. The negative model always produces zero eddy viscosity,  $\nu_t$ .

### 2.3.2. Numerical discretization of the Spalart–Allmaras turbulence model

The Spalart–Allmaras turbulence model is also discretized using spline finite elements. If we let  $\tilde{\nu}_h$  denote numerical approximation of the modified viscosity and define a suitable test function  $\phi_h \in \mathcal{V}_h$ , the method is given as

$$\mathcal{B}^G(\tilde{\nu}_h, \phi_h) = 0, \quad \phi_h \in \mathcal{V}_h^0,$$

where

$$\begin{aligned} \mathcal{B}^G(\tilde{\nu}_h, \phi_h) &= \left( \frac{\partial \tilde{\nu}_h}{\partial t}, \phi_h \right) + c(\mathbf{u}_h; \tilde{\nu}_h, \phi_h) + a(\tilde{\nu}_h, \phi_h) \\ &\quad - s_1(\tilde{\nu}_h, \phi_h) - s_2(\tilde{\nu}_h; \tilde{\nu}_h, \phi_h) + s_3(\tilde{\nu}_h; \tilde{\nu}_h, \phi_h), \end{aligned}$$

and with

$$\begin{aligned} (\tilde{\nu}, \phi) &= \int_{\Omega} \tilde{\nu} \phi \, d\mathbf{x}, \\ c(\mathbf{u}; \tilde{\nu}, \phi) &= (\mathbf{u} \cdot \nabla \tilde{\nu}, \phi), \\ a(\tilde{\nu}, \phi) &= \left( \frac{(\nu + \tilde{\nu})}{\sigma} \nabla \tilde{\nu} \cdot \nabla \phi \right) \\ s_1(\tilde{\nu}, \phi) &= (c_{b1}(1 - f_{t2}) \tilde{S} \tilde{\nu}, \phi), \\ s_2(\tilde{\nu}, \phi) &= \left( \frac{c_{b2}}{\sigma} |\nabla \tilde{\nu}|^2, \phi \right), \\ s_3(\tilde{\nu}, \phi) &= \left( \left( c_{w1} f_w - \frac{c_{b1}}{\kappa} f_{t2} \right) \left[ \frac{\tilde{\nu}}{d} \right]^2, \phi \right). \end{aligned}$$

The negative Spalart–Allmaras model is discretized similarly.

For the temporal discretization we have used a semi-implicit Euler scheme, where the value of  $\tilde{\nu}$  is evaluated at the previous time step  $n$ , i.e.  $\tilde{\nu}^n$  is used, in some of the terms to get a linear problem for the new solution  $\tilde{\nu}^{n+1}$ . More precisely, if  $\Delta t$  is the time step, then the time integration scheme reads

$$\begin{aligned} \left( \frac{\tilde{\nu}^{n+1} - \tilde{\nu}^n}{\Delta t}, \phi \right) + c(\mathbf{u}; \tilde{\nu}^{n+1}, \phi) + a(\tilde{\nu}^n; \tilde{\nu}^{n+1}, \phi) &= s_1(\tilde{\nu}^{n+1}, \phi) \\ &\quad + s_2(\tilde{\nu}^{n+1}, \phi) - s_3(\tilde{\nu}^{n+1}, \phi). \end{aligned}$$

Here the convective term, the diffusion term and all three source terms are treated semi-implicitly. All the coefficients depending on  $\tilde{\nu}$  are evaluated at time level  $n$ .

### 2.3.3. Boundary conditions for the Spalart–Allmaras Model

The Spalart–Allmaras model assumes that the mesh is sufficiently refined close to the wall surfaces with the non-dimensional wall distance  $y^+ \sim 1$ . The non-dimensional wall distance  $y^+$  is defined in terms of the friction velocity  $u_*$  as

$$y^+ = \frac{u_*}{\nu} \quad \text{with} \quad u_* = \sqrt{\frac{\tau_w}{\rho}}$$

where the wall shear stress  $\tau_w$  is given by

$$\tau_w = \mu \left[ \frac{\partial \mathbf{u}}{\partial \mathbf{n}} \right]_{y=0} = \mu [\nabla \mathbf{u} \cdot \mathbf{n}]_{y=0}.$$

Close to the wall the flow is laminar so  $\tilde{\nu}$  is set to zero. On the inflow boundaries  $\tilde{\nu}_{\text{in}} = 5\nu$  is used, whilst a homogeneous Neumann boundary condition is applied on the outflow boundaries and symmetry planes.

$$\frac{\partial \tilde{\nu}}{\partial \mathbf{n}} = \nabla \tilde{\nu} \cdot \mathbf{n} = 0.$$

#### 2.4. Aerodynamic coefficients

The quantities of interest in numerical simulations of flow past an airfoil are the aerodynamic coefficients for a given angle of attack  $\alpha$  and a given Reynolds number  $Re$ . The Reynolds number is defined as

$$Re = \frac{u_\infty c}{\nu},$$

where  $u_\infty$  is the constant inflow velocity,  $c$  is the chord length and  $\nu = \mu/\rho$  is the kinematic viscosity. The three coefficients are the drag coefficient  $C_D$ , the lift coefficient  $C_L$  and the pressure coefficient  $C_P$  defined as

$$C_D = \frac{F_x}{\frac{1}{2}\rho u_\infty^2 cl}, \quad C_L = \frac{F_y}{\frac{1}{2}\rho u_\infty^2 cl}, \quad C_P = \frac{p - p_\infty}{\frac{1}{2}\rho u_\infty^2}.$$

The quantities  $F_x$  and  $F_y$  are the horizontal and vertical force components acting on the airfoil respectively,  $\rho$  is the density of the fluid,  $l$  is the length in the spanwise direction and  $p_\infty$  is the ambient pressure. The force components are computed as

$$\mathbf{F} = [F_x, F_y]^T = \int_{\Gamma_w} \boldsymbol{\sigma} \cdot \mathbf{n} \, ds,$$

where  $\Gamma_w$  is the airfoil surface.

#### 2.5. Mesh generation

Generation of a high quality block-structured mesh can often be a challenge with respect to partitioning the computational domain into 2D quadrilaterals which are not too skewed or distorted. Several other aspects are also relevant. First of all one would like to avoid distorted elements and abrupt change in the element size. Such cases can lead to unwanted grid effects. Secondly, we would like to have smaller elements at parts of the boundary with high curvature and close to solid walls in order to capture boundary layers.

##### 2.5.1. Block-structured mesh generation

A bottom-up approach is often preferred for constructing a block-structured mesh. For two-dimensional problems the procedure can be described as

1. Define the corner nodes for the blocks.
2. Connect the corners to form the edges.
3. Refine the edges with a suitable grading.
4. Connect the edges to form surfaces.

To define the grading of the mesh a geometrical factor  $r$  can be defined as the ratio of the element size of two consecutive elements, i.e. if  $\{\mathbf{x}_i\}_{i=1}^m$  are the points on the edge or curve and  $\Delta s_i = \|\mathbf{x}_i - \mathbf{x}_{i-1}\|_2$  defines the cell size, then

$$r = \Delta s_i / \Delta s_{i-1},$$

for  $i = 2, \dots, m$ . To impose a smooth change in element size, we typically have that  $0.8 < r < 1.2$ , and for sharp boundary layers we may even use  $0.9 < r < 1.1$  to capture the rapid change in the solution.

### 2.5.2. Spline curves

In this section we define spline curves, which form the foundation of the mesh generation, as in [13]. Assume that we have a knot-vector

$$\Xi = \{0 = \xi_1, \xi_2, \dots, \xi_{n+p+1} = 1\}.$$

and a set of control points  $C = \{c_1, \dots, c_n\}$  which defines the spline curve

$$c(\xi) = \sum_{i=1}^n c_i B_{i,p}(\xi),$$

where  $\{B_i\}_{i=1}^n$  are the basis functions. The parameter  $p$  is the polynomial order of the spline curve, and each knot  $\xi_i$  may be repeated several times, but the knot-span should be non-decreasing

$$\xi_1 \leq \xi_2 \leq \dots \leq \xi_{n+p+1}.$$

For  $p = 0$  the basis functions are piecewise constants

$$B_{i,0}(\xi) = \begin{cases} 1, & \xi_i \leq \xi < \xi_{i+1}, \\ 0 & \text{otherwise.} \end{cases}$$

The higher order B-spline basis functions are defined as a linear combination of splines of lower order using the *Cox-de Boor recursion formula*

$$B_{i,p}(\xi) = \frac{\xi - \xi_i}{\xi_{i+p} - \xi_i} B_{i,p-1}(\xi) + \frac{\xi_{i+p+1} - \xi}{\xi_{i+p+1} - \xi_{i+1}} B_{i+1,p-1}(\xi). \quad (3)$$

We restrict our attention to *open* knot-vectors, i.e. splines that are interpolatory at the end points, and then the first and last knots are repeated  $p + 1$  times. Furthermore, if the spline is  $C^{p-1}$  continuous then all the internal knots have multiplicity one and the knot-vector can be written as

$$\Xi = \{\underbrace{\xi_1, \dots, \xi_1}_{p+1}, \xi_2, \dots, \xi_{m-1}, \underbrace{\xi_m, \dots, \xi_m}_{p+1}\},$$

where the number of unique knots is given by  $q = n - p + 1$ . The corresponding knot-vector without repeated knots is

$$\bar{\Xi} = \{\bar{\xi}_1, \bar{\xi}_2, \dots, \bar{\xi}_q\}.$$

### 2.5.3. Cubic spline interpolation

The mesh generation process is dependent on standard cubic spline interpolation [29]. The starting point is a set of  $m$  points  $\{x_i\}_{i=1}^m$  that we want to approximate by a cubic spline curve  $c(\xi)$  such that

- $c(\tilde{\xi}_i) = x_i$  for  $\tilde{\xi}_i \in [0, 1]$ .
- $c(\xi) \in C^2([0, 1])$ .

The points  $\{\tilde{\xi}_i\}_{i=1}^q$  where the spline curve interpolates the data are called the *Greville points*. Two extra conditions are needed to uniquely define the interpolation. We use either Hermitian ( $\mathbf{c}'(0) = \mathbf{t}_0, \mathbf{c}'(1) = \mathbf{t}_1$ ) or natural boundary conditions ( $\mathbf{c}''(0) = \mathbf{c}''(1) = 0$ ), where  $\mathbf{t}_0$  and  $\mathbf{t}_1$  are the tangent vectors of the spline curve at the endpoints. This leads to an  $n \times n$  linear system with  $n = m + 2$ , which can be solved for the unknown control points  $\{\mathbf{c}_i\}_{i=1}^n$ . The interpolation is not uniquely defined since the parametrization can be different.

Cubic spline interpolation is used for the airfoil as given in Equation (1). The entire mesh is made for polynomial order  $p = 3$ , and only lowered to orders  $p = 1$  and  $p = 2$  once all patches and refinements have been completed.

#### 2.5.4. Surface generation

For surface generation we employ the concept of Coons patches [30]. Given four boundary curves  $\mathbf{u}_0(\xi)$ ,  $\mathbf{u}_1(\xi)$ ,  $\mathbf{w}_0(\eta)$ ,  $\mathbf{w}_1(\eta)$  as given in Figure 1. These

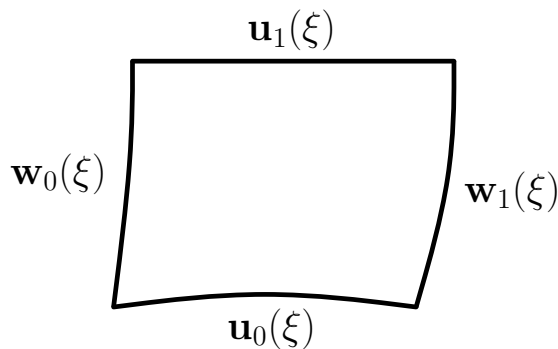


Figure 1: Boundary curves for Coons surface patch.

curves have normalized knot vectors and are connected such that  $\mathbf{u}_0(\xi_1) = \mathbf{w}_0(0)$ ,  $\mathbf{u}_0(1) = \mathbf{w}_1(0)$ ,  $\mathbf{u}_1(1) = \mathbf{w}_1(1)$ ,  $\mathbf{u}_1(0) = \mathbf{w}_0(1)$ , thus forming a closed loop. By defining the surfaces

$$\begin{aligned} S_1(\xi, \eta) &= (1 - \eta)\mathbf{u}_0(\xi) + \eta\mathbf{u}_1(\xi) \\ S_2(\xi, \eta) &= (1 - \eta)\mathbf{w}_0(\eta) + \xi\mathbf{w}_1(\eta) \\ S_3(\xi, \eta) &= (1 - \xi)(1 - \eta)\mathbf{u}_0(0) + \xi(1 - \eta)\mathbf{u}_0(1) + \eta(1 - \xi)\mathbf{u}_1(0) + \xi\eta\mathbf{u}_1(1) \end{aligned}$$

the Coons surface paths is given by

$$S_c(\xi, \eta) = S_1(\xi, \eta) + S_2(\xi, \eta) - S_3(\xi, \eta).$$

The Coons surface patch approach is a quick and easy way of building the surfaces. Being able to define the geometry through the boundary curves of each surface or patch is a great advantage.

### 3. Simulations Setup

A high quality mesh is a prerequisite for a reliable simulation of flow around an aerodynamically shaped body like an airfoil. Here we describe the meshes used for our 2D simulations and the basis for the choice of domain size and time step. Other test cases are also defined.

### 3.1. Mesh description

The meshes are denoted by B followed by an identifying number indicating the level of refinement, i.e. B0 is the coarsest mesh and B2 the finest mesh in our simulations. The meshes are constructed with polynomials of orders 1, 2 and 3, and are intended for use with the Spalart-Allmaras model without any law-of-the-wall parametrization. Each mesh consists of 128 patches, which gives huge flexibility in the number of processors the simulations can be run on. The simulations in this paper are run on 12, 16, 24, 32 or 64 cores. IFEM is parallelized through a domain decomposition approach [31] where each sub-domain consist of one or more patches. The code uses the PETSc [32] for the parallel matrix classes and for the solution of the resulting linear system. The use of PETSc also gives access to iterative (Krylov-type) solution methods and state-of-the-art advanced preconditioners such as algebraic multigrid [33] and additive Schwarz [34]. When it comes to refinement, a basic template given in Figure 2 is used as a starting point. The figure also shows four refinement edges (marked by bold lines) which are used in the mesh generation.

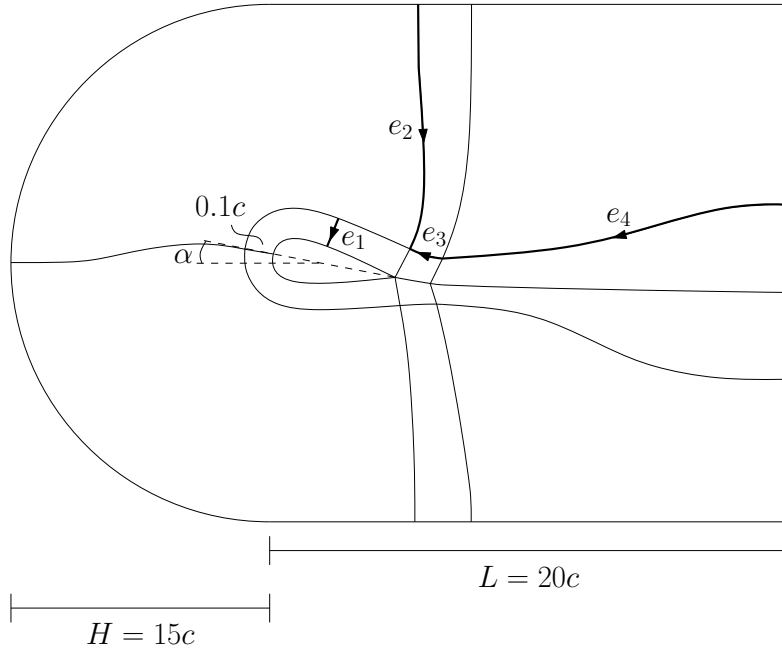


Figure 2: NACA0015: Basic block structure and definition of refinement edges for fixed NACA0015 airfoil with angle of attack  $\alpha$ .

Important refinement parameters for the meshes are presented in Table 1, whilst the grading factors for the different meshes are illustrated in Figure 3. The resulting number of element and degrees-of-freedom are listed in Table 2. Figure 4 shows the B0 mesh for  $\alpha = 6^\circ$  and  $p = 2$ .

In order to evaluate the quality of the meshes we use in our simulations we apply some well-known mesh metrics. The scaled Jacobian mesh metric, described in [35], is shown in Figure 5 for the coarsest grid B0. As can be seen in the figure the scaled Jacobian is positive for all elements, meaning that there should be no unphysical results due to intersecting grid lines. The stretch mesh

Table 1: NACA0015: Detailed refinement information about simulation meshes B0, B1 and B2. Edge grading factor is given by  $r$ , and  $n_{\text{pts}}$  is the number of points along the airfoil surface whilst  $n$  is the number of inserted knots along the given edge.

| Mesh    |                  | B0   | B1   | B2   |
|---------|------------------|------|------|------|
| Airfoil | $n_{\text{pts}}$ | 103  | 127  | 173  |
|         | $r$              | 0.96 | 0.96 | 0.97 |
| $e_1$   | $r$              | 0.81 | 0.89 | 0.92 |
|         | $n$              | 36   | 60   | 80   |
| $e_2$   | $r$              | 0.88 | 0.92 | 0.94 |
|         | $n$              | 35   | 55   | 75   |
| $e_3$   | $r$              | 0.9  | 0.91 | 0.93 |
|         | $n$              | 12   | 18   | 24   |
| $e_4$   | $r$              | 0.89 | 0.92 | 0.94 |
|         | $n$              | 35   | 50   | 65   |

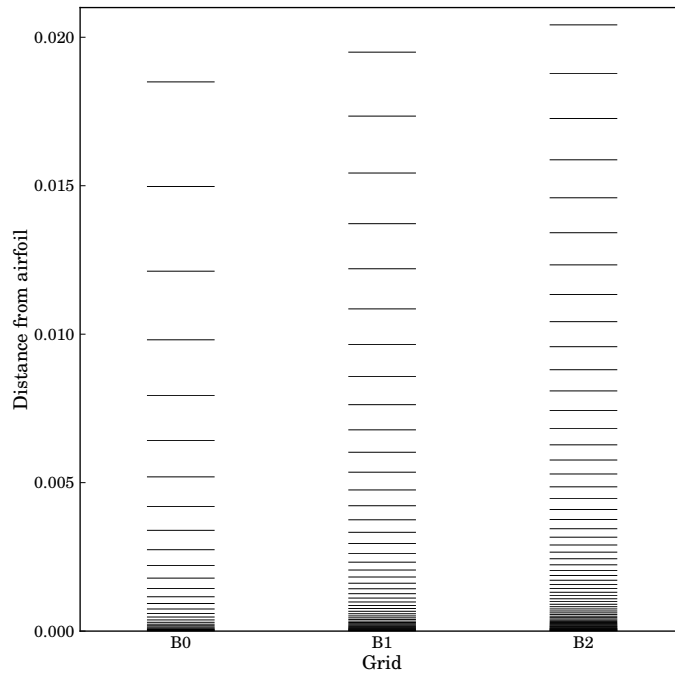


Figure 3: NACA0015: Grading factor illustration (zoomed) of the innermost patches close to the airfoil for the different meshes.

metric is shown in Figure 6. The IFEM solver is able to handle large element aspect ratios.

Table 2: NACA0015: Number of elements and degrees-of-freedom for simulation meshes B0, B1 and B2 and polynomial orders  $p = 1, 2, 3$ .

| Mesh | $p$ | $n_{\text{el}}$ | $n_{\text{dof}}$ |
|------|-----|-----------------|------------------|
| B0   | 1   | 22046           | 67116            |
|      | 2   | 22046           | 78222            |
|      | 3   | 22046           | 90096            |
| B1   | 1   | 45864           | 138909           |
|      | 2   | 45864           | 155319           |
|      | 3   | 45864           | 172497           |
| B2   | 1   | 82582           | 249522           |
|      | 2   | 82582           | 271380           |
|      | 3   | 82582           | 294006           |

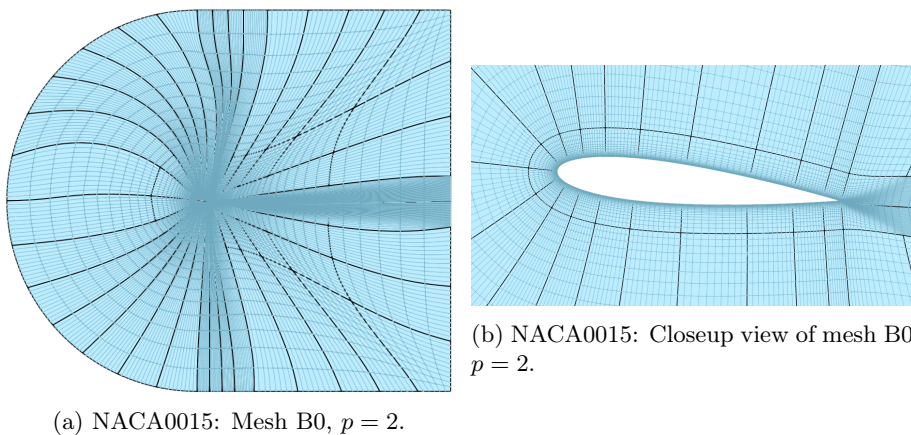


Figure 4: NACA0015: Grid B0 for  $\alpha = 6^\circ$ . Patch boundaries in black.

### 3.2. Physical parameters and boundary conditions

All simulations are based on a fluid density of  $\rho = 1.205 \text{ kg/m}^3$ , dynamic viscosity  $\mu = 1.8208 \times 10^{-5} \text{ kg/(m s)}$  and inflow velocity  $u_\infty = 37.775 \text{ m/s}$  giving a Reynolds number of  $Re = 2.5 \times 10^6$ . An inlet boundary condition is imposed on the curved surface, a wall boundary condition is imposed on the airfoil surface, a slip condition is applied on the lateral boundaries while a homogeneous Neumann condition is used for the outflow.

### 3.3. Determination of the domain size

In the simulation of the kind presented in the paper one expects the aerodynamic coefficients of the airfoil to be independent of the location of the boundaries. Sensitivity studies were conducted to identify the domain extent. Basically the dimensions  $L$  and  $H$  (Figure 2) were varied and simulations for five different domain extents (B1, K0, K1, K2, K3) were conducted to compute the drag and lift coefficients. The specifications of the domain set-ups are given in Table 3. In all the five setups the airfoil is discretized using  $n = 127$  points along the surface with a grading factor of  $r = 0.96$  towards both the trailing and the

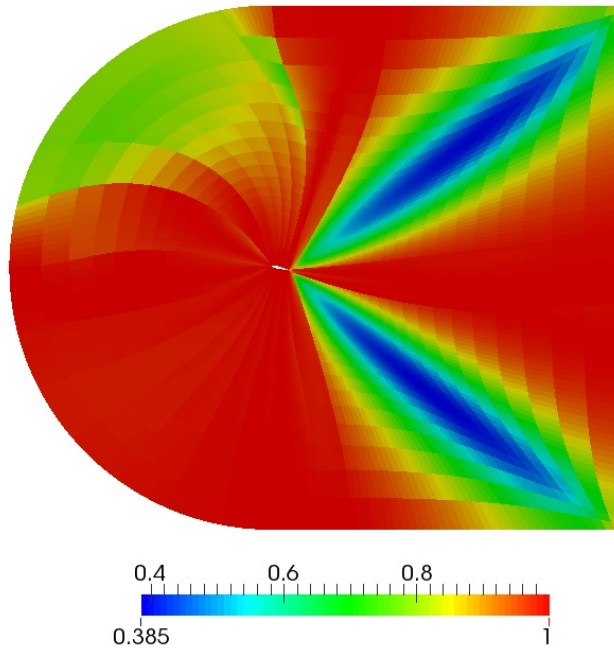


Figure 5: NACA0015: Scaled Jacobian mesh metric for grid B0 at  $12^\circ$  angle of attack.

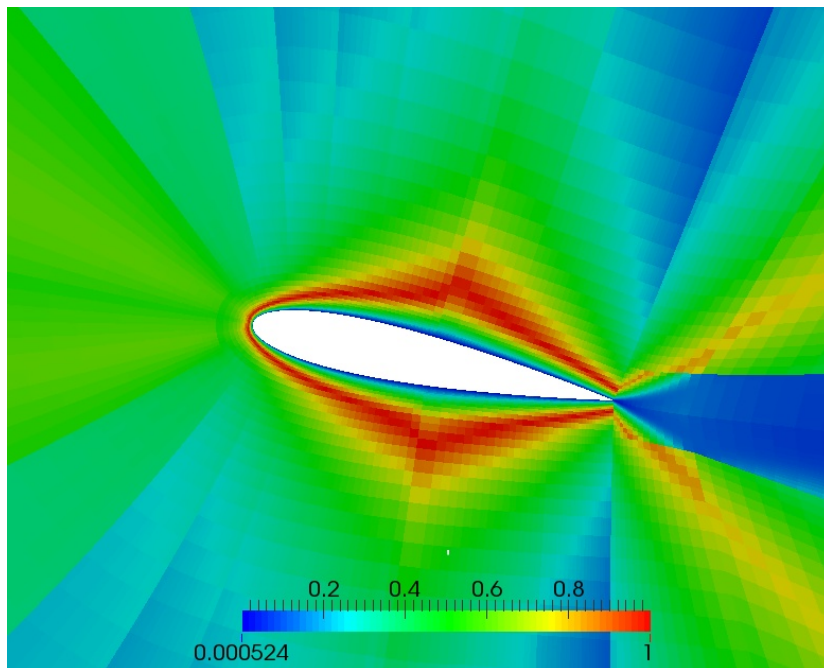


Figure 6: NACA0015: Stretch mesh metric for grid B0 at  $12^\circ$  angle of attack.

leading edges. All the simulations were conducted for an angle of attack  $\alpha = 6^\circ$ , order  $p = 1$  and until a non-dimensional time  $t = 50$ . The results for drag and

lift coefficients are shown in Table 4. The sixth and the seventh column in the table shows the percentage error in  $C_L$  and  $C_D$  associated with the changes in the domain size with respect to B1. The percentage change in any case is less than 2.5% which should be acceptable for all practical purposes. We thus fix the B1 domain configuration for subsequent analysis. The chosen domain setup is shown in Figure 7.

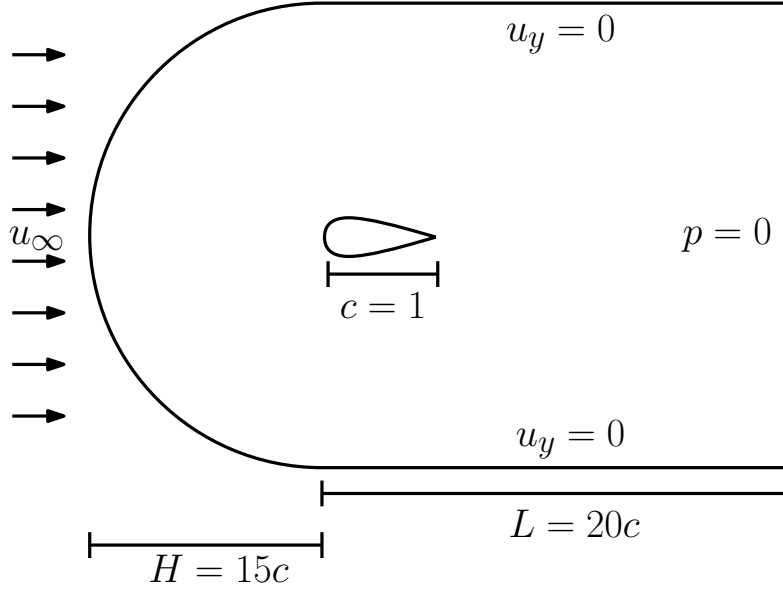


Figure 7: NACA0015: Computational domain for fixed NACA0015 airfoil.

Table 3: NACA0015: Details of mesh and domain size. Edge grading factor is given by  $r$ , whilst  $n$  is the number of inserted knots.

| Grid      |     | B1     | K0     | K1     | K2     | K3     |
|-----------|-----|--------|--------|--------|--------|--------|
| $H$       |     | $15c$  | $15c$  | $15c$  | $10c$  | $20c$  |
| $L$       |     | $20c$  | $15c$  | $30c$  | $20c$  | $20c$  |
| $n_{el}$  |     | 45864  | 44694  | 47736  | 43120  | 47824  |
| $n_{dof}$ |     | 138909 | 135384 | 144549 | 130656 | 144804 |
| $e_1$     | $r$ | 0.89   | 0.89   | 0.89   | 0.89   | 0.89   |
|           | $n$ | 60     | 60     | 60     | 60     | 60     |
| $e_2$     | $r$ | 0.92   | 0.92   | 0.92   | 0.92   | 0.92   |
|           | $n$ | 55     | 55     | 55     | 48     | 60     |
| $e_3$     | $r$ | 0.91   | 0.91   | 0.91   | 0.91   | 0.91   |
|           | $n$ | 18     | 18     | 18     | 18     | 18     |
| $e_4$     | $r$ | 0.92   | 0.92   | 0.925  | 0.92   | 0.92   |
|           | $n$ | 50     | 45     | 58     | 50     | 50     |

Based on the small variations in the lift and drag coefficient a problem area size of  $H = 15c$  and  $L = 20c$  is chosen.

Table 4: NACA0015: Results for flow past a NACA0015 airfoil at  $\alpha = 12^\circ$  with  $p = 1$ .

| Grid | $p$ | $\Delta t$ | $\alpha = 12^\circ$ |         | $\frac{ C_L - C_{L,B1} }{C_{L,B1}}$ [%] | $\frac{ C_D - C_{D,B1} }{C_{D,B1}}$ [%] |
|------|-----|------------|---------------------|---------|---|---|
|      |     |            | $C_L$               | $C_D$   |   |   |
| B1   | 1   | 0.0005     | 1.21490             | 0.02352 | -                                       | -                                       |
| K0   | 1   | 0.0005     | 1.20620             | 0.02407 | 0.72                                    | 2.31                                    |
| K1   | 1   | 0.0005     | 1.21041             | 0.02317 | 0.37                                    | 1.49                                    |
| K2   | 1   | 0.0005     | 1.21011             | 0.02387 | 0.39                                    | 1.46                                    |
| K3   | 1   | 0.0005     | 1.20820             | 0.02355 | 0.55                                    | 0.10                                    |

### 3.4. Time step determination

In order to determine a sufficiently small time step several simulations were run on the finest grid, B2, with a sufficiently small time step  $\Delta t = 0.0005$  or  $\Delta t = 0.00035$  and spline elements of order  $p = 1$ ,  $p = 2$  and  $p = 3$  for three angles of attack. All simulations were run to non-dimensional time  $t = 75$ , equaling 150000 or approximately 214000 time steps. The results are shown in Table 5. As all simulations converge it can be safely concluded that the Courant-Friedrichs-Lewy (CFL) condition, which is necessary for stability, is satisfied. All subsequent simulations were therefore conducted with time step given in Table 5.

Table 5: NACA0015: Results for grid B2 in determination of the time step  $\Delta t$ .

|           | Grid | $p$ | $\alpha$ [°] | $\Delta t$ | $C_L$    | $C_D$   |
|-----------|------|-----|--------------|------------|----------|---------|
| IFEM (SA) | B2   | 1   | 0            | 0.0005     | -0.00016 | 0.01041 |
| IFEM (SA) | B2   | 1   | 6            | 0.0005     | 0.64573  | 0.01299 |
| IFEM (SA) | B2   | 1   | 12           | 0.0005     | 1.21902  | 0.02286 |
| IFEM (SA) | B2   | 2   | 0            | 0.0005     | 0.00001  | 0.01046 |
| IFEM (SA) | B2   | 2   | 6            | 0.0005     | 0.63758  | 0.01298 |
| IFEM (SA) | B2   | 2   | 12           | 0.0005     | 1.20819  | 0.02276 |
| IFEM (SA) | B2   | 3   | 0            | 0.0005     | -0.00003 | 0.01047 |
| IFEM (SA) | B2   | 3   | 6            | 0.0005     | 0.63409  | 0.01301 |
| IFEM (SA) | B2   | 3   | 12           | 0.00035    | 1.20745  | 0.02187 |

### 3.5. Simulation length

In order to determine the lift and drag parameters it is crucial that the simulations are run until a quasi steady-state situation is achieved. This is monitored through the cumulative lift and drag coefficients. A time history plot of the cumulative mean of the lift and drag coefficients for grid B0,  $p = 2$ ,  $\alpha = 12^\circ$  and  $\Delta t = 0.0005$  is shown in Figure 8.

Based on these results, the calculations of the lift and drag coefficients are based on the time interval between 70 and 75 ( $\approx 10000$  time steps).

### 3.6. Definition of test cases

Once the domain size, time steps and simulation length are established further simulations were conducted for three mesh setups B0, B1, B2 with linear,

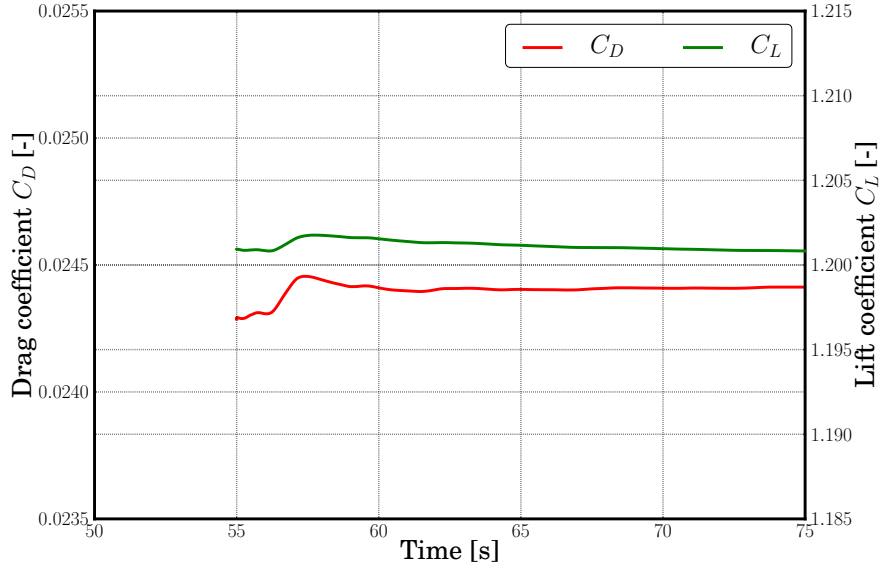


Figure 8: NACA0015: Cumulative mean of  $C_L$  and  $C_D$  at  $\alpha = 12^\circ$  for grid B0,  $p = 2$ ,  $\Delta t = 0.0005$ .

quadratic and cubic spline elements with a time step as given in Table 5. All inputs, including boundary conditions, are identical for all the cases with an angle of attack  $\alpha = 0^\circ, 6^\circ, 12^\circ$ . Thus a total of 27 cases are investigated.

#### 4. Results and discussion

Results from the 27 different cases discussed in the previous section are now compared against two sets of experimental ([36],[37]) results. While the results in [37] come from the experiments conducted at the same Reynolds number as in this paper, the results in [36] were obtained from wind tunnel experiments conducted at lower Reynolds numbers and then extended to higher ones. In the following subsections we present and discuss our 2D simulation results for different angles of attack  $\alpha$ .

##### 4.1. Results for $\alpha = 0^\circ$

An angle of attack of  $\alpha = 0^\circ$  corresponds to a situation where the flow is expected to be statistically symmetric and absence of any flow separation. Experimental values of nearly zero lift therefore does not come as a surprise. The pressure field in Figure 21a computed by numerical simulation is symmetric about the chord line which implies that the pressure integrated over the top surface and bottom surface will be equal in magnitude and opposite in direction resulting in a net zero lift. Also the flow impinges on the leading edge resulting in a relatively high pressure zone on this side of the flow and hence a positive drag coefficient.

#### 4.1.1. Lift and drag coefficients for $\alpha = 0^\circ$

Lift and drag coefficients for  $\alpha = 0^\circ$  are shown in Table 6 along with experimental results available in the literature. The results are also presented in Figure 9. Lift coefficients are predicted very well in our simulations and compare well to the two sets of experimental results. Drag coefficients on the other hand are overpredicted. This is as expected due to the use of the Spalart-Allmaras turbulence model which assumes fully turbulent flow. However, drag coefficients seem to be better approximated for  $p = 1$  than for  $p = 2$  and  $p = 3$ , whilst lift coefficients seem to be better approximated with increasing spline element order  $p$ .

#### 4.1.2. Surface pressure plots for $\alpha = 0^\circ$

The surface pressure coefficients for mesh B2 and  $p = 1, 2, 3$  computed using IFEM are compared against experimental results from [37] in Figure 10. Figures 11 and 12 give a zoomed-in view of the  $C_p$  plot towards the leading and trailing edges respectively. The comparisons for  $p = 1, p = 2$  and  $p = 3$  are in good agreement.

### 4.2. Results for $\alpha = 6^\circ$

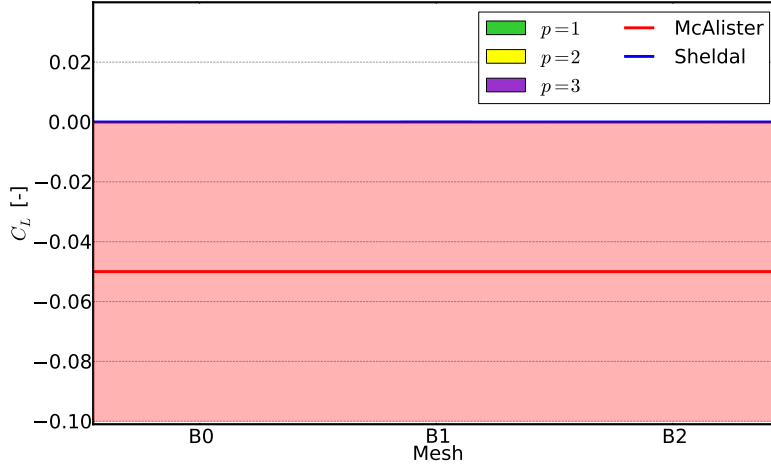
As the angle of attack increases to  $\alpha = 6^\circ$  the flow becomes asymmetric. Figure 21b shows that a relatively large surface area now tries to obstruct the flow resulting in the development of high pressure zone on the bottom-leading side of the airfoil. The asymmetric distribution of the pressure on the airfoil results not only in a net upward lift but also a positive drag force. The experiments confirm the results.

#### 4.2.1. Lift and drag coefficients for $\alpha = 6^\circ$

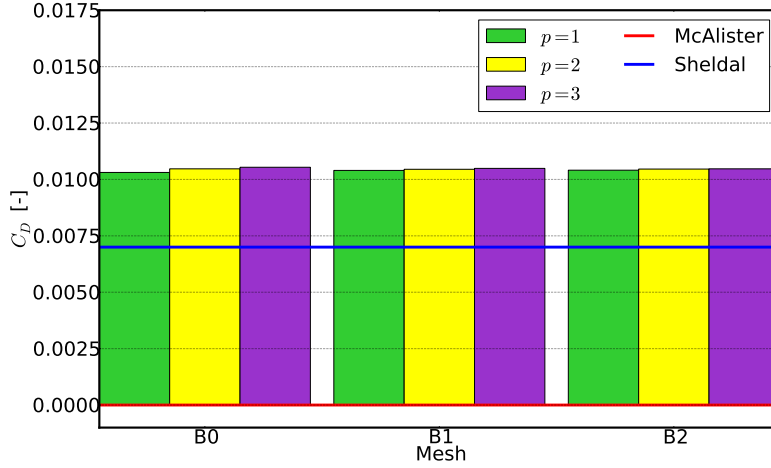
For  $\alpha = 6^\circ$ , lift and drag coefficients are shown in Table 7 along with experimental results available in the literature. The results are also presented in Figure 13. The drag coefficients seem to be somewhat higher than the experimental results. This overprediction is again due to the Spalart-Allmaras turbulence model assuming fully turbulent flow. Again, drag coefficients for

Table 6: NACA0015: Lift and drag coefficients for flow past a fixed NACA0015 airfoil at  $\alpha = 0^\circ$  and  $Re = 2.5 \times 10^6$ .

|                            | Grid | $p$ | $\Delta t$ | $C_L$        | $C_D$   |
|----------------------------|------|-----|------------|--------------|---------|
| IFEM (SA)                  | B0   | 1   | 0.0005     | -0.00009     | 0.01031 |
| IFEM (SA)                  | B0   | 2   | 0.0005     | 0.00001      | 0.01047 |
| IFEM (SA)                  | B0   | 3   | 0.0005     | -0.00005     | 0.01054 |
| IFEM (SA)                  | B1   | 1   | 0.0005     | 0.00007      | 0.01040 |
| IFEM (SA)                  | B1   | 2   | 0.0005     | 0.00020      | 0.01045 |
| IFEM (SA)                  | B1   | 3   | 0.0005     | 0.00000      | 0.01049 |
| IFEM (SA)                  | B2   | 1   | 0.0005     | -0.00016     | 0.01041 |
| IFEM (SA)                  | B2   | 2   | 0.0005     | 0.00001      | 0.01046 |
| IFEM (SA)                  | B2   | 3   | 0.0005     | -0.00003     | 0.01047 |
| Exp: McAlister et al. [37] |      |     |            | -0.01 - 0.00 | 0.00    |
| Exp: Sheldal et al. [36]   |      |     |            | 0.000        | 0.0070  |



(a) Lift coefficients ( $\alpha = 0^\circ$ ).



(b) Drag coefficients ( $\alpha = 0^\circ$ ).

Figure 9: NACA0015: Lift and drag coefficients for flow past a fixed NACA0015 airfoil at  $\alpha = 0^\circ$  and  $Re = 2.5 \times 10^6$ .

$p = 2$  and  $p = 3$  are higher than for  $p = 1$ . The lift coefficients obtained for all three grids are closer to the experiments in [36] than in [37]. Lift coefficients obtained with  $p = 1$  are lower than for  $p = 2$  and  $p = 3$ .

#### 4.2.2. Surface pressure plots for $\alpha = 6^\circ$

Surface pressure coefficient plots for IFEM runs with the Spalart-Allmaras turbulence model are presented in Figure 14 for grid B2, alongside comparisons with surface pressure distributions from experiments in [37]. Figure 15 and 16 once again gives a zoomed in view of the  $C_p$  plot towards the leading and trailing edges respectively. In this case, even for sufficiently fine mesh the coefficients are not accurately predicted towards both the edges. There are only minor differences in the  $C_p$ -curves for different polynomial orders.

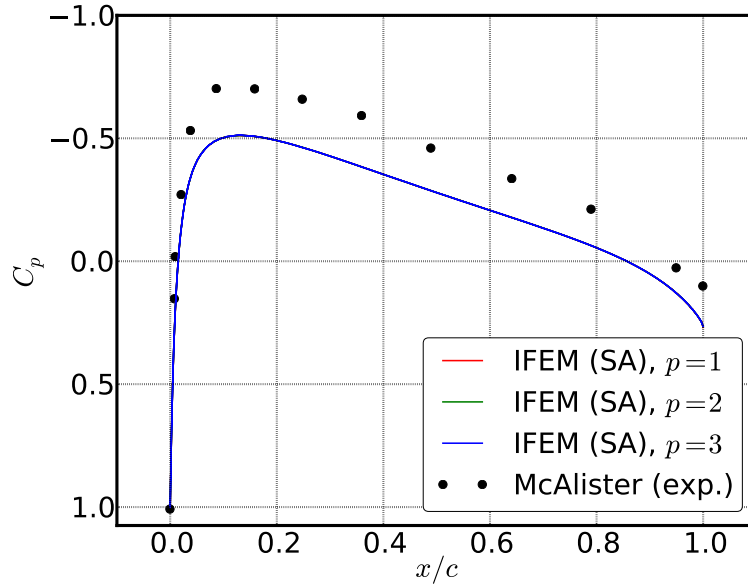


Figure 10: NACA0015: Surface pressure plot for  $\alpha = 0^\circ$ . Simulation run for grid B2 with  $p = 1$ ,  $p = 2$  and  $p = 3$ ,  $\Delta t = 0.0005$ .

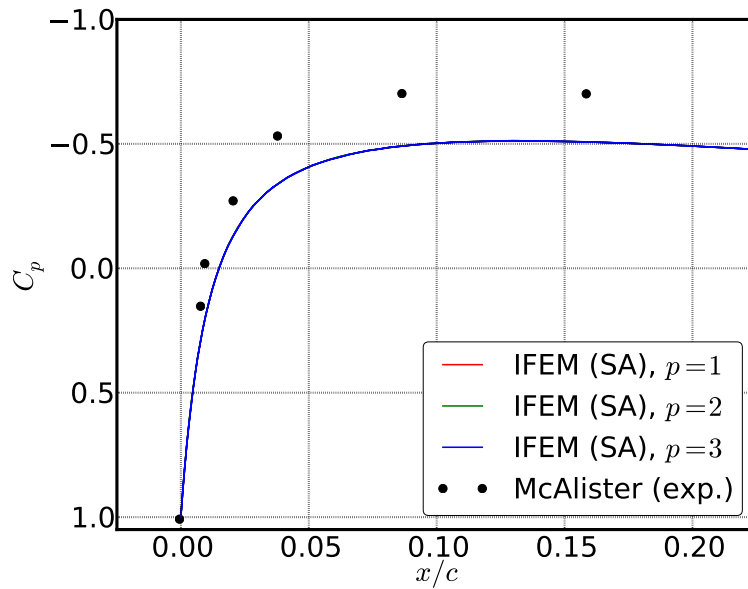


Figure 11: NACA0015: Surface pressure plot of leading edge for  $\alpha = 0^\circ$ . Simulation run for grid B2 with  $p = 1$ ,  $p = 2$  and  $p = 3$ ,  $\Delta t = 0.0005$ .

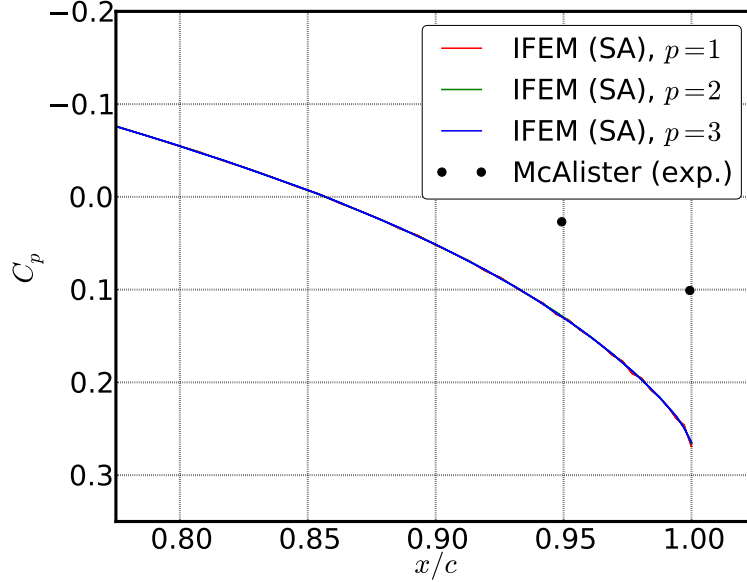


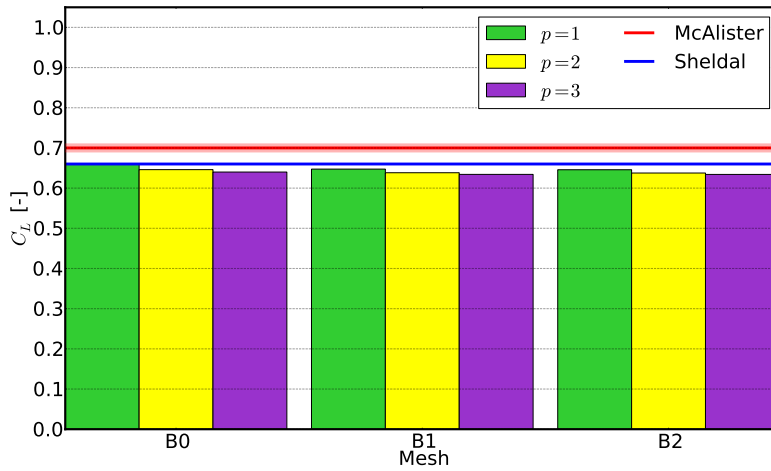
Figure 12: NACA0015: Surface pressure plot of trailing edge for  $\alpha = 0^\circ$ . Simulation run for grid B2 with  $p = 1$ ,  $p = 2$  and  $p = 3$ ,  $\Delta t = 0.0005$ .

Table 7: NACA0015: Lift and drag coefficients for flow past a fixed NACA0015 airfoil at  $\alpha = 6^\circ$  and  $Re = 2.5 \times 10^6$ .

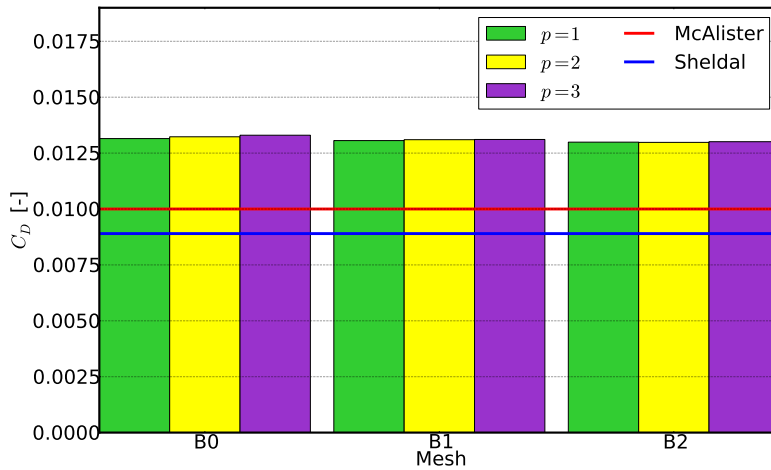
|                             | Grid | $p$ | $\Delta t$ | $C_L$       | $C_D$   |
|-----------------------------|------|-----|------------|-------------|---------|
| IFEM (SA)                   | B0   | 1   | 0.0005     | 0.66101     | 0.01315 |
| IFEM (SA)                   | B0   | 2   | 0.0005     | 0.64599     | 0.01323 |
| IFEM (SA)                   | B0   | 3   | 0.0005     | 0.64000     | 0.01330 |
| IFEM (SA)                   | B1   | 1   | 0.0005     | 0.64732     | 0.01306 |
| IFEM (SA)                   | B1   | 2   | 0.0005     | 0.63829     | 0.01310 |
| IFEM (SA)                   | B1   | 3   | 0.0005     | 0.63419     | 0.01311 |
| IFEM (SA)                   | B2   | 1   | 0.0005     | 0.64573     | 0.01299 |
| IFEM (SA)                   | B2   | 2   | 0.0005     | 0.63758     | 0.01298 |
| IFEM (SA)                   | B2   | 3   | 0.0005     | 0.63409     | 0.01301 |
| Exp: McAlistier et al. [37] |      |     |            | 0.69 - 0.71 | 0.01    |
| Exp: Sheldal et al. [36]    |      |     |            | 0.660       | 0.0089  |

#### 4.3. Results for $\alpha = 12^\circ$

As the angle of attack is further increased to  $\alpha = 12^\circ$  more of the bottom surface of the airfoil is exposed to the incident flow and hence higher pressure. Contrary to that, the top surface is shielded from the incident flow and hence relatively much lower pressure is experienced. As in the previous case it results in positive lift and drag forces albeit much bigger in magnitude. Once again the prediction is confirmed by experimental observations.



(a) Lift coefficients ( $\alpha = 6^\circ$ ).



(b) Drag coefficients ( $\alpha = 6^\circ$ ).

Figure 13: NACA0015: Lift and drag coefficients for flow past a fixed NACA0015 airfoil at  $\alpha = 6^\circ$  and  $Re = 2.5 \times 10^6$ .

#### 4.3.1. Lift and drag coefficients for $\alpha = 12^\circ$

Lift and drag coefficients for  $\alpha = 12^\circ$  are shown in Table 8 along with experimental results available in the literature. The results are also presented in Figure 17. The drag coefficients are once again overpredicted compared to the experimental results. For the lift coefficients the differences between  $p = 1$  on the one hand and  $p = 2$  and  $p = 3$  on the other are more pronounced than for lower angles of attack. Lift coefficients are in between the experimental results in [36] and [37] and thus show reasonable agreement.

#### 4.3.2. Surface pressure plots for $\alpha = 12^\circ$

Surface pressure coefficient plots for IFEM run with the Spalart-Allmaras turbulence model are presented in Figure 18, alongside comparisons with surface pressure distributions from experiments in [37].

As for the two lower angles of attack, there are only minor differences in the prediction of pressure coefficients along the whole airfoil when using spline

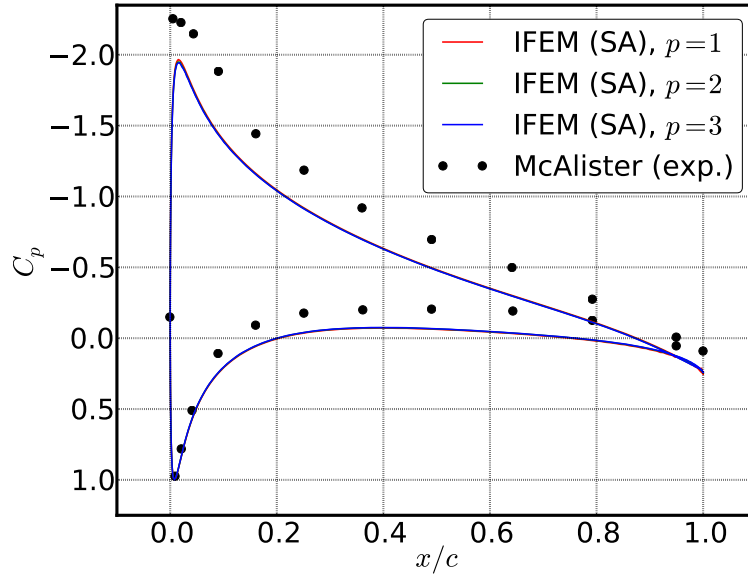


Figure 14: NACA0015: Surface pressure plot for  $\alpha = 6^\circ$ . Simulation run for grid B2 with  $p = 1$ ,  $p = 2$  and  $p = 3$ ,  $\Delta t = 0.0005$ .

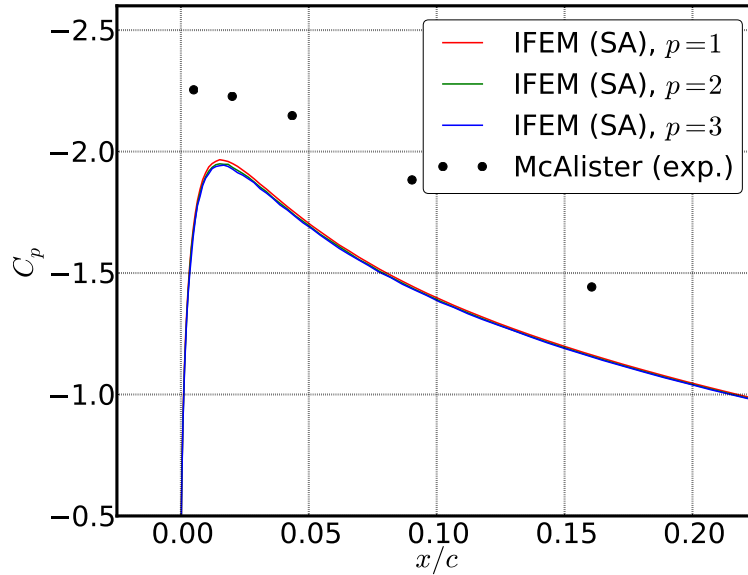


Figure 15: NACA0015: Surface pressure plot of leading edge for  $\alpha = 6^\circ$ . Simulation run for grid B2 with  $p = 1$ ,  $p = 2$  and  $p = 3$ ,  $\Delta t = 0.0005$ .

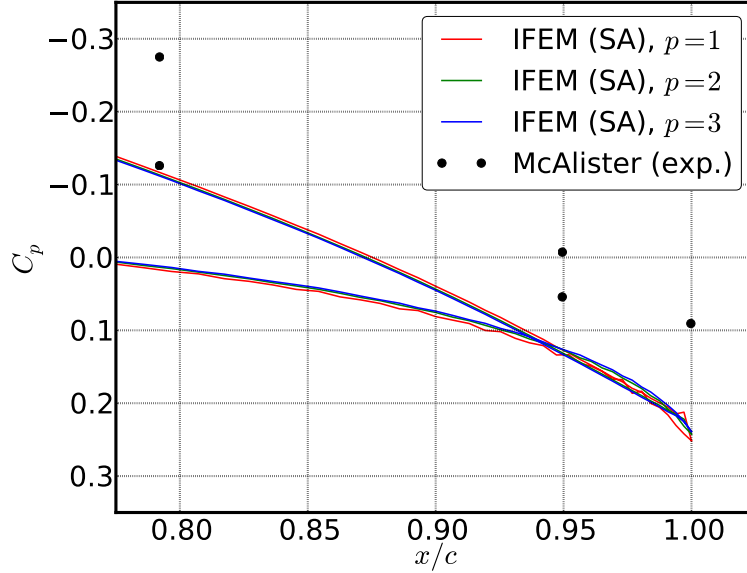


Figure 16: NACA0015: Surface pressure plot of trailing edge for  $\alpha = 6^\circ$ . Simulation run for grid B2 with  $p = 1$ ,  $p = 2$  and  $p = 3$ ,  $\Delta t = 0.0005$ .

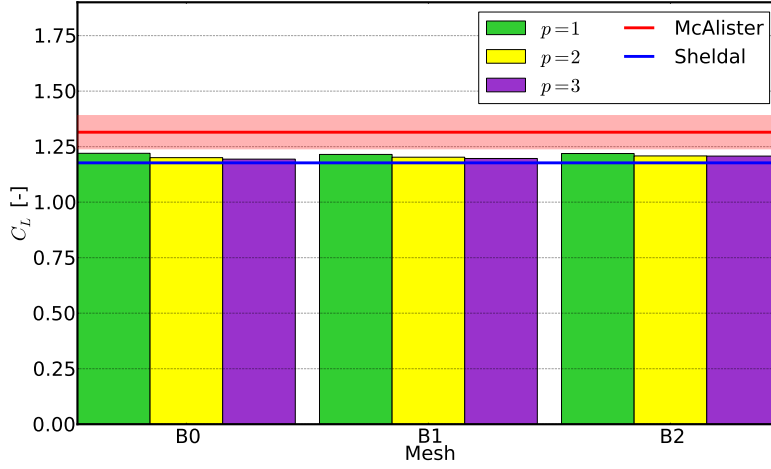
Table 8: NACA0015: Lift and drag coefficients for flow past a fixed NACA0015 airfoil at  $\alpha = 12^\circ$  and  $Re = 2.5 \times 10^6$ .

|                            | Grid | $p$ | $\Delta t$ | $C_L$       | $C_D$       |
|----------------------------|------|-----|------------|-------------|-------------|
| IFEM (SA)                  | B0   | 1   | 0.0005     | 1.22001     | 0.02446     |
| IFEM (SA)                  | B0   | 2   | 0.0005     | 1.20042     | 0.02443     |
| IFEM (SA)                  | B0   | 3   | 0.0005     | 1.19376     | 0.02451     |
| IFEM (SA)                  | B1   | 1   | 0.0005     | 1.21490     | 0.02352     |
| IFEM (SA)                  | B1   | 2   | 0.0005     | 1.20243     | 0.02344     |
| IFEM (SA)                  | B1   | 3   | 0.0005     | 1.19667     | 0.02343     |
| IFEM (SA)                  | B2   | 1   | 0.0005     | 1.21902     | 0.02286     |
| IFEM (SA)                  | B2   | 2   | 0.0005     | 1.20819     | 0.02276     |
| IFEM (SA)                  | B2   | 3   | 0.00035    | 1.20745     | 0.02187     |
| Exp: McAlister et al. [37] |      |     |            | 1.24 - 1.39 | 0.03 - 0.06 |
| Exp: Sheldal et al. [36]   |      |     |            | 1.177       | 0.0157      |

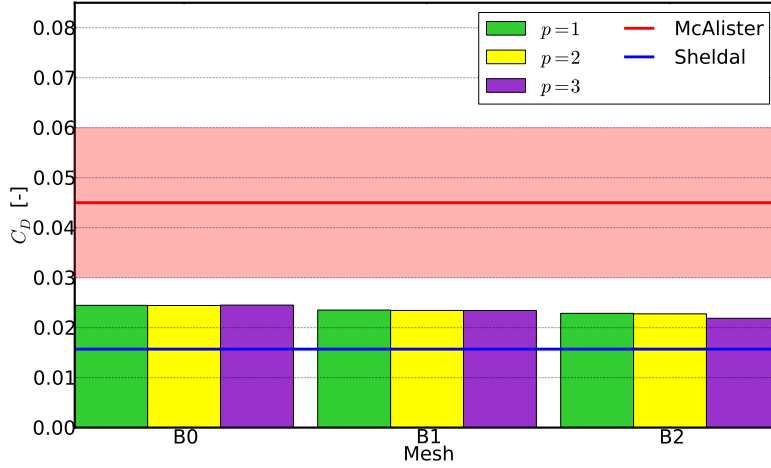
elements of order polynomial order  $p = 1, 2, 3$ .

#### 4.4. Low $Re$ investigations

As all results presented so far have shown only little or no improvement for the surface pressure distributions with increasing spline element order, we make some additional investigations at a low Reynolds number,  $Re = 250$ . This is done for two grids. The first is B0 as presented earlier, with a distance to the first knotline designed for  $y^+ = 1$  at  $Re = 2.5 \times 10^6$ . The other is B3, much coarser than grids B0-B2 and designed for  $Re = 250$ , with 10890 elements. Distance



(a) Lift coefficients ( $\alpha = 12^\circ$ ).



(b) Drag coefficients ( $\alpha = 12^\circ$ ).

Figure 17: NACA0015: Lift and drag coefficients for flow past a fixed NACA0015 airfoil at  $\alpha = 12^\circ$  and  $Re = 2.5 \times 10^6$ .

to the first knotline for B3 is  $0.2/\sqrt{(Re)}$ , and all investigations are carried out at an angle of attack  $\alpha = 12^\circ$ . The resulting surface pressure distributions are shown in Figure 22. From the figure it is clear that polynomial order has an impact only for grid B3, not for grid B0 which is designed to resolve the boundary layer for  $Re = 2.5 \times 10^6$ . The significant difference is between linear elements on the one side and quadratic and cubic elements on the other.

## 5. Conclusions

The major contribution of this work has been the demonstration of the usage of a Navier-Stokes solver based on an isogeometric finite element method using a Chorin projection method and Spalart-Allmaras turbulence model to simulate high Reynolds number flow ( $Re = 2.5 \times 10^6$ ) around the NACA0015 airfoil

for three different angles of attack. Also, another original contribution is the design of meshes for isogeometric computation of airfoil flows. Most significant

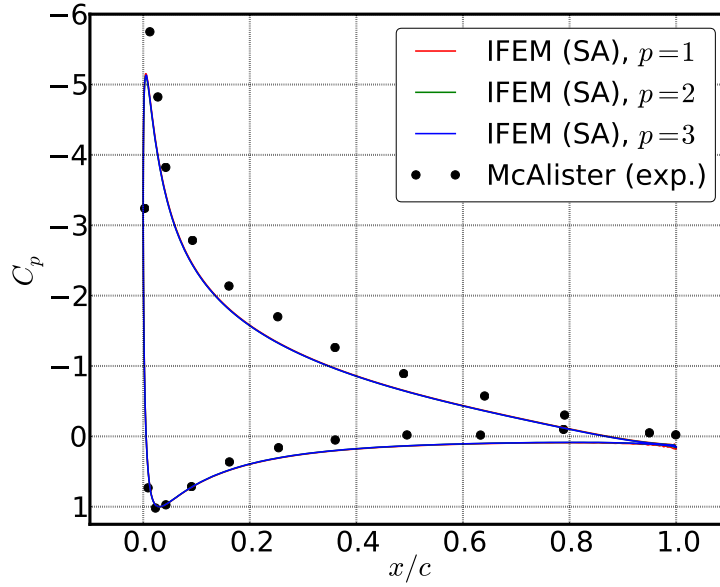


Figure 18: NACA0015: Surface pressure plot for  $\alpha = 12^\circ$ . Simulation run for grid B2 with  $p = 1$ ,  $p = 2$  and  $p = 3$ ,  $\Delta t = 0.0005$  for  $p = 1, 2$ ,  $\Delta t = 0.00035$  for  $p = 3$ .

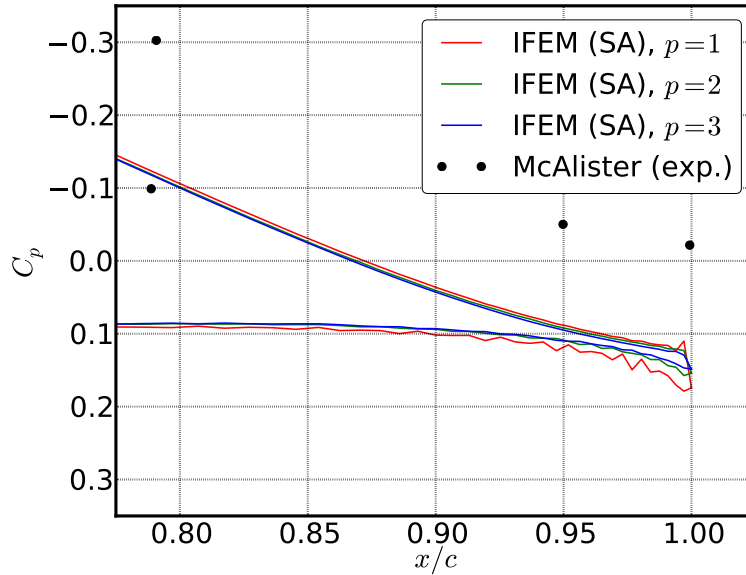


Figure 19: NACA0015: Surface pressure plot of trailing edge for  $\alpha = 12^\circ$ . Simulation run for grid B2 with  $p = 1$ ,  $p = 2$  and  $p = 3$ ,  $\Delta t = 0.0005$  for  $p = 1, 2$ ,  $\Delta t = 0.00035$  for  $p = 3$ .

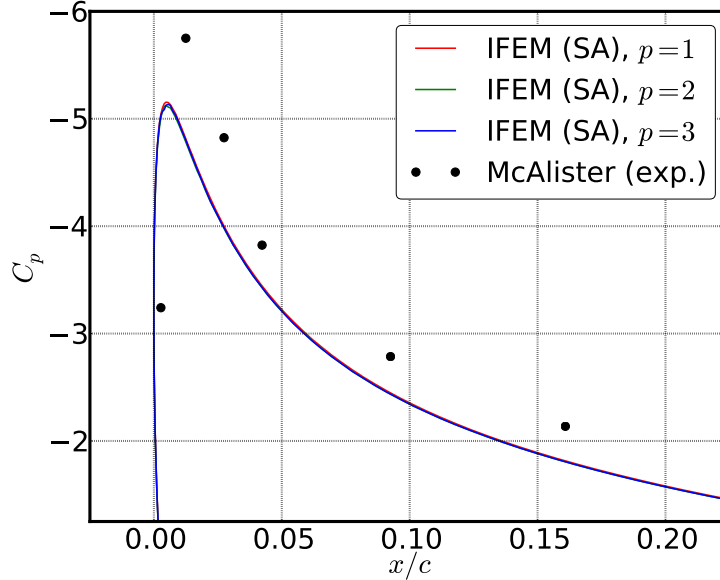
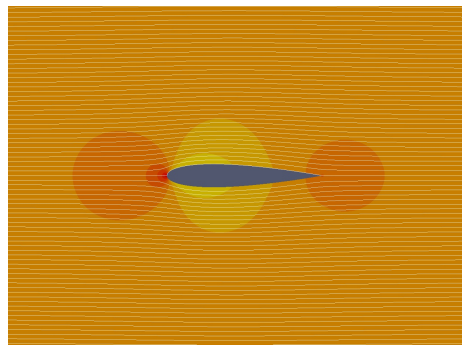


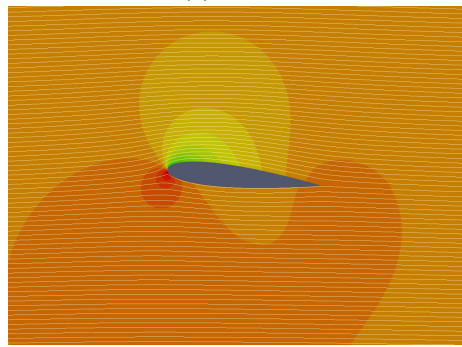
Figure 20: NACA0015: Surface pressure plot of leading edge for  $\alpha = 12^\circ$ . Simulation run for grid B2 with  $p = 1$ ,  $p = 2$  and  $p = 3$ ,  $\Delta t = 0.0005$  for  $p = 1, 2$ ,  $\Delta t = 0.00035$  for  $p = 3$ .

concluding remarks are enumerated as follows:

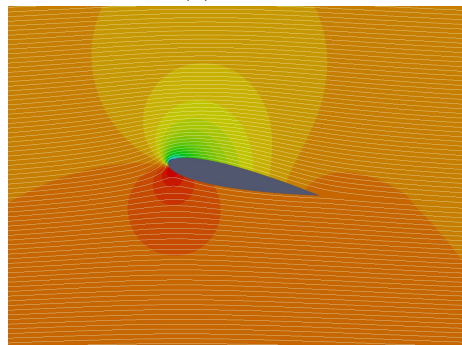
- The solver presented computes lift, drag and pressure coefficients which are in reasonable agreement with the experimental observations. The pressure coefficients were underpredicted for all the angles of attack.
- The work also investigates in detail and comes up with a choice of domain size, mesh resolution, time step and simulation length for the flow investigated.
- It gets increasingly more difficult numerically to predict drag, lift and pressure coefficients with increasing angle of attack.
- There is very little benefit evident from the usage of higher order splines, particularly for prediction of  $C_p$ .
- It appears that the gain in numerical accuracy is more than offset by the modeling error associated with RANS-based turbulence modeling approach. This is perhaps the reason no improvement in accuracy was observed when the simulations were conducted with high Reynolds number and Spalart-Allmaras turbulence model. On the contrary, at low Reynolds number when no turbulence model was activated, the added value due to higher order splines was observed for the coarse mesh. This explanation can be taken to argue in favor of a turbulence resolving approach in comparison to a turbulence modeling approach.
- The numerical results have been compared to experimental observations which can itself have errors associated with them which have not been



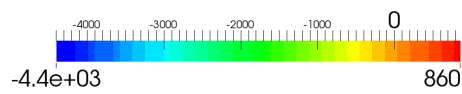
(a)  $\alpha = 0^\circ$



(b)  $\alpha = 6^\circ$



(c)  $\alpha = 12^\circ$

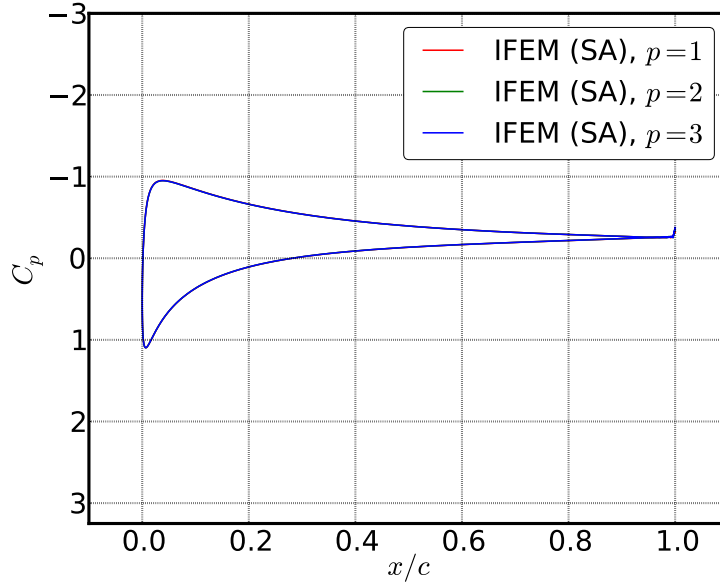


(d) Common legend

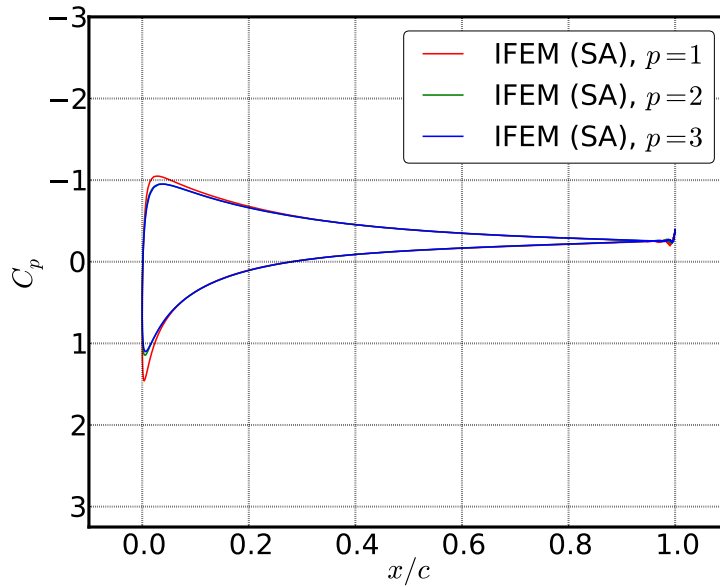
Figure 21: NACA0015: Pressure contours with streamlines around the airfoil for different angles of attack.

taken into account while a comparison is being made. There is definitely a need for more accurate experiments with quantified uncertainties and errors.

- In spite of some shortfalls the results from our study give a promising



(a) Grid B0,  $Re = 250$ ,  $\alpha = 12^\circ$



(b) Grid B3,  $Re = 250$ ,  $\alpha = 12^\circ$

Figure 22: NACA0015: Surface pressure distributions for  $Re = 250$ .

outlook for further work towards fluid-structure interaction simulations of wind turbine blades using the developed isogeometric finite element Navier-Stokes solver IFEM. The possibility to use RANS-based turbulence

model in addition to VMS and LES can make the methodology attractive to a wider community, many of whom will be interested in quick results. In particular, 2D airfoil sections as studied here can be coupled through a beam element in a strip theory approach as in [10] and [8].

However, flow around an airfoil, particularly at higher angles of attack, is characterized by three-dimensional flow phenomena like vorticity fluctuation and vortex stretching. A combination of a RANS approach and two-dimensional simulations suppresses all the three-dimensional flow phenomena. Even in three-dimensional flow simulations, owing to the diffusive nature of any RANS model, these phenomena will remain unresolved. An LES or VMS approach will be more suited to accurately model such flow. Weak enforcement of boundary conditions, such as in [38], appears a promising proposition as it is computationally less demanding and stable compared to the more conventional approach.

## 6. Acknowledgment

The authors acknowledge the financial support from the Norwegian Research Council and the industrial partners of *NOWITECH: Norwegian Research Centre for Offshore Wind Technology* (grant no: 193823/S60) (<http://www.nowitech.no>) and *FSI-WT* (grant no: 216465/E20) (<http://www.fsi-wt.no>). Furthermore, the authors greatly acknowledge the *Norwegian metacenter for computational science* (NOTUR-reference number: NN9322K/1589) ([www.notur.no](http://www.notur.no)) for giving us access to the *Vilje* high performance computer at the Norwegian University of Science and Technology (NTNU).

## References

- [1] EWEA, Wind in our sails, Tech. rep., European Wind Energy Association (2011).
- [2] EWEA, Wind in power - 2013 European statistics, Tech. rep., European Wind Energy Association (2014).
- [3] M. Hansen, J. Sørensen, S. Voutsinas, N. Sørensen, H. Madsen, State of the art in wind turbine aerodynamics and aeroelasticity, *Progress in Aerospace Sciences* 42 (4) (2006) 285–330.
- [4] M.-C. Hsu, Y. Bazilevs, Fluid-structure interaction modeling of wind turbines: Simulating the full machine, *Computational Mechanics* 50 (6) (2012) 821–833.
- [5] Y. Bazilevs, M.-C. Hsu, J. Kiendl, R. Wüchner, K.-U. Bletzinger, 3D simulation of wind turbine rotors at full scale. Part II: Fluid-structure interaction modeling with composite blades, *International Journal for Numerical Methods in Fluids* 65 (1-3) (2011) 236–253.
- [6] C. B. Jenssen, T. Kvamsdal, K. M. Okstad, J. Amundsen, Parallel methods for fluid-structure interaction, in: B. Kågström, J. Dongarra, E. Elmroth, J. Waśniewski (Eds.), *Applied Parallel Computing Large Scale Scientific and Industrial Problems*, Vol. 1541 of *Lecture Notes in Computer Science*, Springer Berlin Heidelberg, 1998, pp. 263–274.
- [7] C. B. Jenssen, T. Kvamsdal, Computational methods for FSI-simulations of slender bridges on high performance computers, in: T. Kvamsdal (Ed.), *Computational Methods for Fluid-Structure Interactions*, Tapir Publisher, Trondheim, 1999, pp. 31–40.
- [8] T. Kvamsdal, C. B. Jenssen, K. M. Okstad, J. Amundsen, Fluid-structure interactions for structural design, in: T. Kvamsdal (Ed.), *Computational Methods for Fluid-Structure Interactions*, Tapir Publisher, Trondheim, 1999, pp. 211–238.
- [9] I. Enevoldsen, C. Pederson, S. Hansen, L. Thorbek, T. Kvamsdal, Computational wind simulations for cable-supported bridges, in: A. Larsen (Ed.), *Wind Engineering into the 21st Century*, Vol. 2, Balkema, Rotterdam, The Netherlands, 1999, pp. 1265–1270.
- [10] K. Herfjord, S. O. Drange, T. Kvamsdal, Assessment of vortex-induced vibrations on deepwater risers by considering fluid-structure interaction, *Journal of Offshore Mechanics and Arctic Engineering* 121 (4) (1999) 207–212.
- [11] K. Herfjord, G. Olsen, T. Kvamsdal, K. M. Okstad, Fluid-Structure Interaction in the case of Two Independent Cylinders in Vortex Induced Vibrations (VIV), *International Journal of Applied Mechanics and Engineering* 7 (2002) 65–83.
- [12] T. Hughes, J. Cottrell, Y. Bazilevs, Isogeometric analysis: CAD, finite elements, NURBS, exact geometry and mesh refinement, *Computer Methods in Applied Mechanics and Engineering* 194 (39-41) (2005) 4135–4195.

- [13] J. A. Cottrell, T. J. Hughes, Y. Bazilevs, *Isogeometric analysis: toward integration of CAD and FEA*, Wiley, Chichester, 2009.
- [14] Y. Bazilevs, M.-C. Hsu, I. Akkerman, S. Wright, K. Takizawa, B. Henicke, T. Spielman, T. Tezduyar, 3D simulation of wind turbine rotors at full scale. Part I: Geometry modeling and aerodynamics, *International Journal for Numerical Methods in Fluids* 65 (1-3) (2011) 207–235.
- [15] Y. Bazilevs, M.-C. Hsu, M. Scott, Isogeometric fluid-structure interaction analysis with emphasis on non-matching discretizations, and with application to wind turbines, *Computer Methods in Applied Mechanics and Engineering* 249-252 (2012) 28–41.
- [16] K. Takizawa, D. Montes, S. McIntyre, T. Tezduyar, Space-time VMS methods for modeling of incompressible flows at high Reynolds numbers, *Mathematical Models and Methods in Applied Sciences* 23 (2) (2013) 223–248.
- [17] K. Nordanger, R. Holdahl, A. M. Kvarving, A. Rasheed, T. Kvamsdal, Implementation and comparison of three isogeometric Navier-Stokes solvers applied to simulation of flow past a fixed 2D NACA0012 airfoil at high Reynolds number, *Computer Methods in Applied Mechanics and Engineering* 284 (2015) 664–688.
- [18] P. Spalart, S. Allmaras, One-equation turbulence model for aerodynamic flows, *Recherche aerospaciale* 1 (1994) 5–21.
- [19] K. Valen-Sendstad, A. Logg, K.-A. Mardal, H. Narayanan, M. Mortensen, A Comparison of Some Common Finite Element Schemes for the Incompressible Navier-Stokes Equations, Vol. 84 of *Lecture Notes in Computational Science and Engineering*, Springer, 2012, Ch. 21, pp. 395–418.
- [20] P. Mineev, A stabilized incremental projection scheme for the incompressible Navier-Stokes equations, *International Journal for Numerical Methods in Fluids* 36 (4) (2001) 441–464.
- [21] E. N. Jacobs, K. E. Ward, R. M. Pinkerton, The characteristics of 78 related airfoil sections from tests in the variable-density wind tunnel, Tech. rep., National Advisory Committee for Aeronautics (1933).
- [22] F. Brezzi, On the existence, uniqueness and approximation of saddle-point problems arising from Lagrangian multipliers, *Rev. Francaise Automat. Informat. Recherche Operationelle Ser Rouge* 8.
- [23] A. J. Chorin, Numerical solution of the Navier-Stokes equations, *Mathematics of Computation* 22 (1968) 745–762.
- [24] R. Temam, Sur l’approximation de la solution des equations de navier-stokes par la methode des pas fractionnaires (ii), *Archive for Rational Mechanics and Analysis* 33 (5) (1969) 377–385.
- [25] J. Guermond, P. Mineev, J. Shen, An overview of projection methods for incompressible flows, *Computer Methods in Applied Mechanics and Engineering* 195 (44-47) (2006) 6011–6045.

- [26] L. Timmermans, P. Mineev, F. Van De Vosse, An approximate projection scheme for incompressible flow using spectral elements, *International Journal for Numerical Methods in Fluids* 22 (7) (1996) 673–688.
- [27] J. Guermond, J. Shen, On the error estimates for the rotational pressure-correction projection methods, *Mathematics of Computation* 73 (248) (2004) 1719–1737.
- [28] S. R. Allmaras, F. T. Johnson, P. R. Spalart, Modifications and clarifications for the implementation of the Spalart-Allmaras turbulence model, in: *ICCFD7 Proceedings*, 2012.
- [29] R. Bartels, J. Beatty, B. Barsky, *An Introduction to Splines for Use in Computer Graphics and Geometric Modeling*, Morgan Kaufmann Series in Computer Graphics and Geometric Modeling, Morgan Kaufmann, 1987.
- [30] S. A. Coons, *Surfaces for computer-aided design of space forms*, Tech. Rep. MAC-TR-41, Cambridge, MA, USA (1967).
- [31] B. Smith, P. Bjørstad, W. Gropp, *Domain Decomposition: Parallel Multi-level Methods for Elliptic Partial Differential Equations*, Cambridge University Press, 2004.
- [32] S. Balay, S. Abhyankar, M. F. Adams, J. Brown, P. Brune, K. Buschelman, V. Eijkhout, W. D. Gropp, D. Kaushik, M. G. Knepley, L. C. McInnes, K. Rupp, B. F. Smith, H. Zhang, *PETSc Web page*, <http://www.mcs.anl.gov/petsc> (2014).
- [33] M. Heroux, R. Bartlett, V. Howle, R. Hoekstra, J. Hu, T. Kolda, R. Lehoucq, K. Long, R. Pawlowski, E. Phipps, A. Salinger, H. Thornquist, R. Tuminaro, J. Willenbring, A. Williams, K. Stanley, An overview of the Trilinos project, *ACM Transactions on Mathematical Software* 31 (3) (2005) 397–423.
- [34] Y. Saad, *Iterative Methods for Sparse Linear Systems*, 2nd Edition, Society for Industrial and Applied Mathematics, Philadelphia, PA, USA, 2003.
- [35] P. Knupp, Achieving finite element mesh quality via optimization of the Jacobian matrix norm and associated quantities. Part II - A framework for volume mesh optimization and the condition number of the Jacobian matrix, *International Journal for Numerical Methods in Engineering* 48 (8) (2000) 1165–1185.
- [36] R. E. Sheldal, P. C. Klimas, Aerodynamic characteristics of seven symmetrical airfoil sections through 180-degree angle of attack for use in aerodynamic analysis of vertical axis wind turbines, Tech. Rep. SAND80-2114, Sandia National Laboratories (March 1981).
- [37] K. W. McAlister, R. K. Takahashi, NACA 0015 wing pressure and trailing vortex measurements, NASA Technical Paper 3151, National Aeronautics and Space Administration, aVSCOM technical report 91-A-003 (1991).
- [38] Y. Bazilevs, T. Hughes, Weak imposition of Dirichlet boundary conditions in fluid mechanics, *Computers and Fluids* 36 (1) (2007) 12–26.